Supplementary Materials for

Self-assembly of magnetite nanocubes into helical superstructures

Gurvinder Singh, Henry Chan, Artem Baskin, Elijah Gelman, Nikita Repnin, Petr Král,* Rafal Klajn*

*Corresponding author. E-mail: rafal.klajn@weizmann.ac.il (R.K.); pkral@uic.edu (P.K.)

This PDF file includes:

Materials and Methods

Figs. S1 to S28

References

Supplementary Materials

Materials and Methods

S1. Nanocrystal synthesis

S1A. Preparation of monodisperse cubic Fe₃O₄ nanocrystals

Fe₃O₄ nanocubes were prepared by thermal decomposition of iron (III) oleate in the presence of sodium oleate, according to a modified literature procedure (*16*). First, iron oleate was prepared as follows: iron (III) chloride hexahydrate (Alfa Aesar, 98%) (5.40 g; 19.98 mmol) and sodium oleate (TCI, >97%) (18.25 g; 59.95 mmol) were placed in a 250 mL round-bottom flask containing 30 mL of distilled water, 70 mL of hexane and 40 mL of ethanol. The mixture was vigorously stirred at $T = 70$ °C under nitrogen atmosphere for four hours. The dark red organic phase was collected with a separatory funnel, washed three times with distilled water, and dried over magnesium sulfate. The solvent was evaporated *in vacuo* at 50-60 °C to yield viscous, dark brown liquid. The product was kept frozen at $T \approx -5$ °C.

As-prepared iron oleate (1.57 g; 1.75 mmol), sodium oleate (TCI, >97%) (0.53 g; 1.74 mmol), and *n*-docosane (6.0 g; 19.32 mmol, Aldrich, 99%) were placed in a 50 mL round-bottom flask containing 11 mL of 1-octadecene (Aldrich, 90%). The reaction mixture was heated to 120 °C to dissolve all solids, and kept under high vacuum for 40 minutes. The reaction mixture was then heated to $T = 325$ °C with a heating rate of 3 °C / min under nitrogen atmosphere, and left at this temperature for 26 minutes with vigorous stirring. The heating source was then removed and the reaction mixture was cooled down to $T = 80$ °C. Nanocrystals were precipitated upon the addition of a mixture composed of 2 volumes of *n*-hexane and 3 volumes of ethanol (with respect to the original solution volume). The clear supernatant was discarded and the solids were redispersed in *n*-hexane and re-precipitated with a small amount of methanol with the help of a neodymium magnet. Re-precipitating with a magnet was repeated two more times. Finally, the solid product was dried under vacuum, and finally redispersed in toluene. Yield = 60-70 mg. The resulting nanocubes had an average side length, $d = 13.37$ nm.
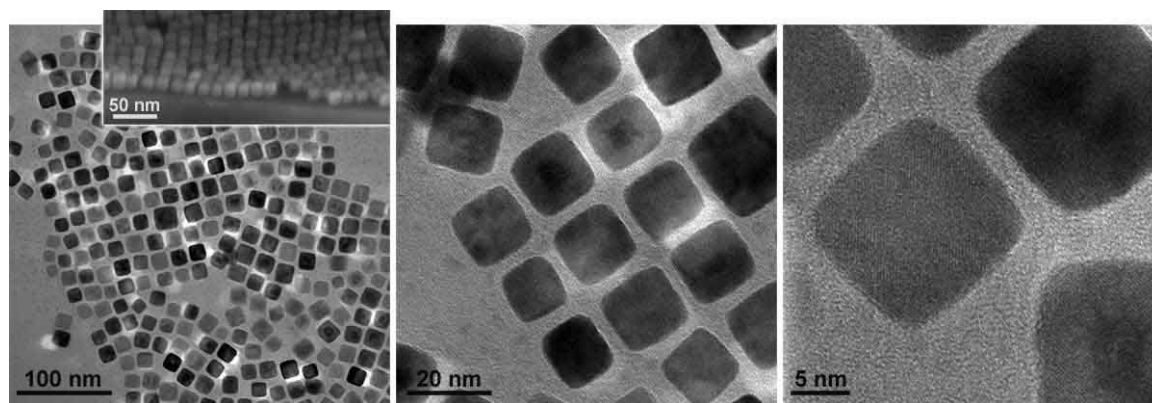

Fig. S1. TEM and SEM (inset) images of Fe₃O₄ nanocubes at various magnifications. All TEM images shown in this manuscript were obtained on a Philips CM120 Super Twin microscope operating at 120 kV unless noted otherwise.
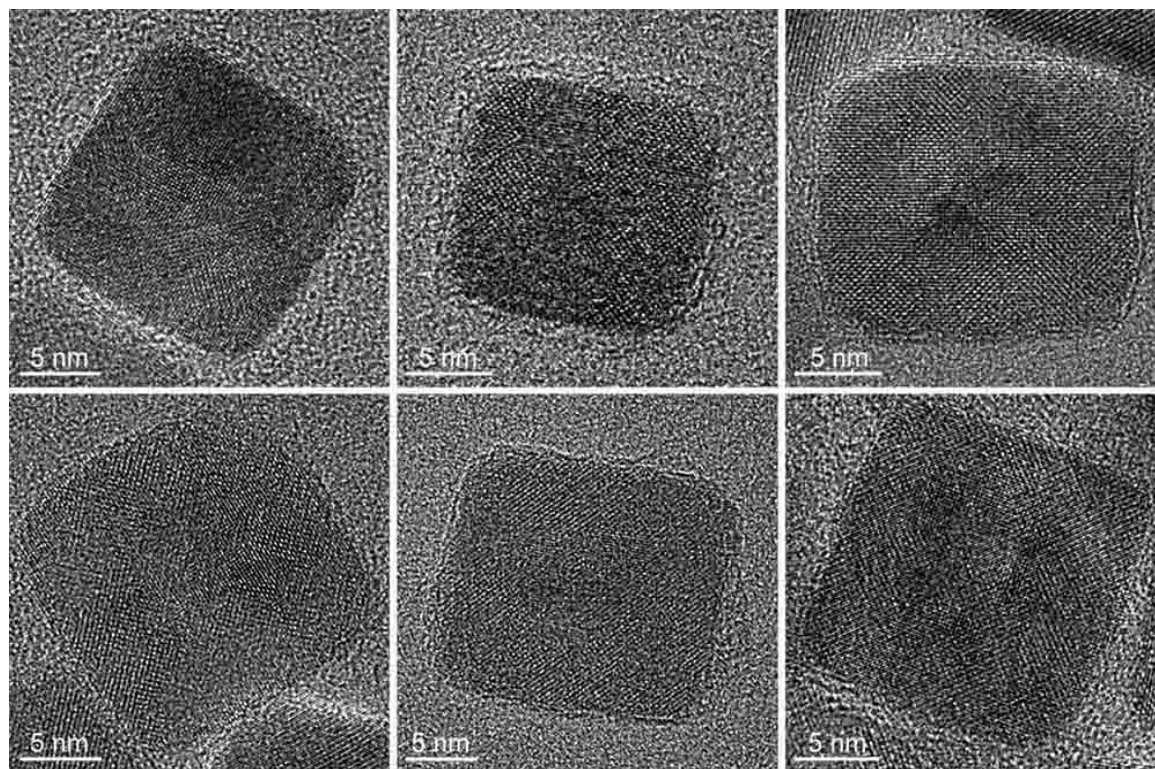
Fig. S2. High-resolution (HR) TEM images of Fe$_3$O$_4$ nanocubes at various magnifications. HR TEM images were taken using an FEI Tecnai F30 UT microscope operating at 300 kV. The micrographs were acquired by a Gatan Ultrascan 1000 CCD camera.
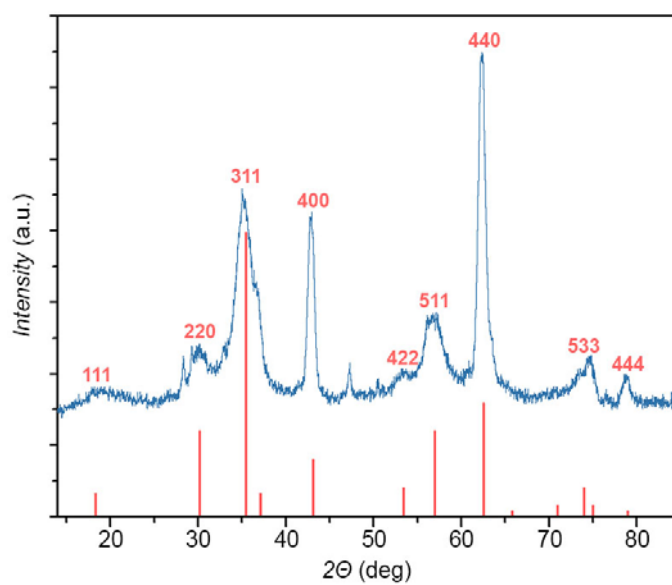

Fig. S3. *Blue*: Powder X-ray diffractogram of as-prepared Fe$_3$O$_4$ nanocubes. *Red*: standard XRD data for Fe$_3$O$_4$ (JCPDS file 19-0629).

S1B. Preparation of monodisperse spherical Fe_3O_4 nanocrystals

Fe_3O_4 nanospheres were prepared by thermal decomposition of iron (III) oleate, according to a literature procedure (*38*). Iron oleate (1.600 g; 1.78 mmol) and oleic acid (0.6 mL; 1.89 mmol) were dissolved in 25 mL of 1-octadecene (Aldrich, 90%). The solution was heated with a constant heating rate of 3 °C / min to $T = 310$ °C under nitrogen atmosphere and vigorous stirring. The reaction mixture was kept at reflux for 30 min and then the heating source was removed. After cooling down to room temperature, the nanocrystals were precipitated with a mixture of solvents composed of hexane, isopropanol and acetone ($v/v/v = 1:2:2$ with respect to the original solution volume). The transparent supernatant was discarded, the solids were washed twice with a mixture composed of 0.5 volume of hexane and 1 volume of acetone (with respect to the original solution volume), collected by centrifugation, dried *in* vacuo and finally redissolved in toluene. The resulting nanospheres had an average diameter, $d \approx 12$ nm.
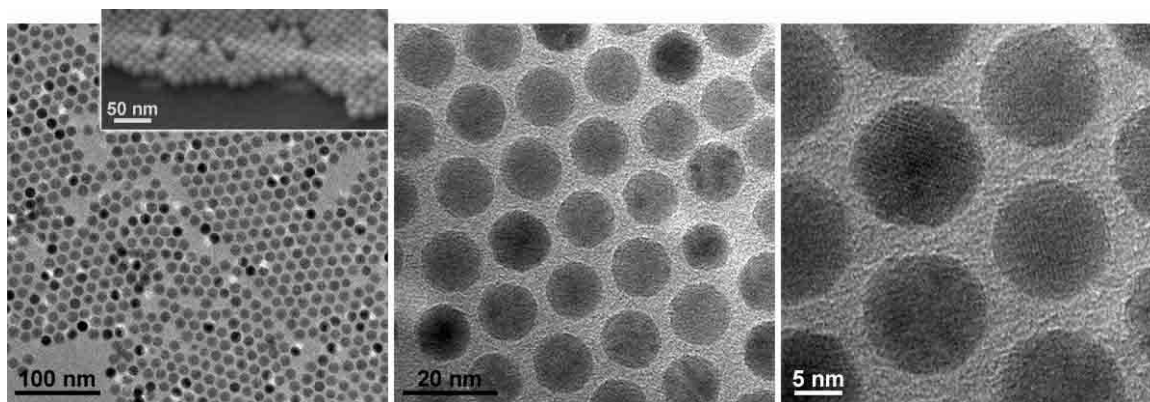

Fig. S4. TEM and SEM (inset) images of Fe_3O_4 nanospheres at various magnifications.

S1C. Preparation of monodisperse octahedral Fe_3O_4 nanocrystals

Fe_3O_4 nanooctahedra were synthesized from as-prepared spherical Fe_3O_4 NCs (Section S1B). 50 mg of nanospheres were precipitated from a toluene solution with methanol, dried, and redispersed in 3 mL hexane containing 0.5 µL of oleic acid. The resulting solution was added to 15 mL of 1-octadecene (Aldrich, 90%) containing sodium oleate (TCI, >97%) (65 mg; 0.22 mmol). The temperature of the solution was raised to $T = 140$ °C with a constant heating rate of 4 °C / min, and kept under high vacuum for 20 minutes to remove residual hexane. The reaction mixture was then heated to reflux ($T = 318$ °C) with a constant heating rate of 5 °C / min and kept at this temperature for 40 minutes under nitrogen atmosphere. After cooling down to room temperature, NCs were precipitated with a mixture composed of hexane, *n*-butanol and acetone ($v/v/v = 1:2:2$ with respect to the original solution volume) with centrifugation. The solids were redissolved in hexane and re-precipitated with acetone. This step was repeated two times, and dried solid product was dispersed in toluene.
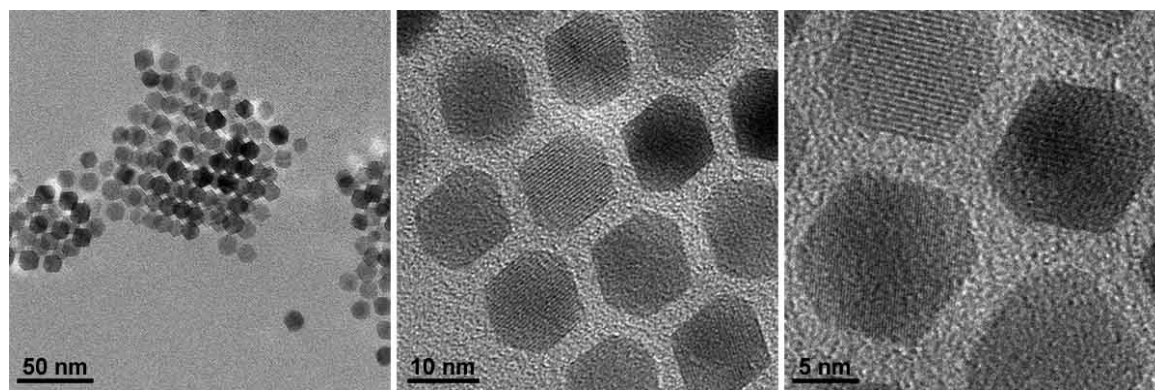
Fig. S5. TEM images of Fe_3O_4 nanooctahedra at various magnifications.

S1D. Preparation of monodisperse Fe_3O_4 rounded cubes

Iron (III) oleate (1.57 g) and sodium oleate (TCI, >97%) (0.53 g) were dissolved in 1-octadecene (7.5 mL) containing 4.5 g of *n*-docosane. The temperature of the vigorously stirred solution was raised to $T = 120$ °C with a constant heating rate of 10 °C / min, and kept under high vacuum for 40 minutes. The reaction mixture was then heated to $T = 325$ °C with a constant heating rate of 3 °C / min and kept at this temperature for 20 minutes under nitrogen atmosphere. The heating source was then removed and the reaction mixture was cooled down to $T = 80$ °C. Nanocrystals were precipitated upon the addition of a mixture composed of 2 volumes of *n*-hexane and 3 volumes of ethanol (with respect to the original solution volume). The clear supernatant was discarded and the solids were redispersed in *n*-hexane and re-precipitated with ethanol. The solid product was dried under vacuum, and finally redispersed in toluene.
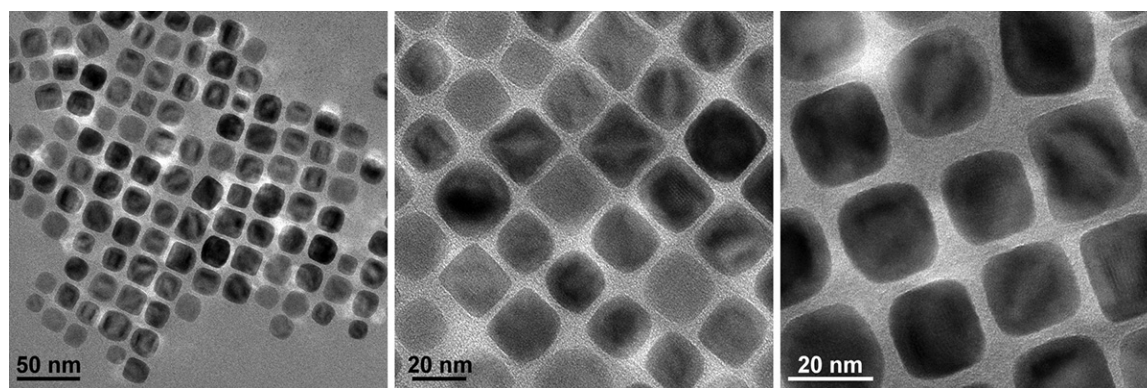

Fig. S6. TEM images of Fe_3O_4 rounded cubes at various magnifications.

S1E. Preparation of heterodimeric Ag-Fe_3O_4 nanoparticles

Ag-Fe_3O_4 heterodimeric NPs were prepared based on a modified literature procedure (*39*). In a typical synthesis, silver acetate (20 mg; 0.12 mmol) was dissolved in 10 mL of toluene

containing 730 µL (2.22 mmol) of oleylamine (Aldrich, 70%) and then Fe_3O_4 nanocubes (10 mg) were added. Following the addition of *n*-dodecanethiol (Aldrich, >98%) (0.44 µL; 1.83 µmol), the solution was heated at 70 °C under nitrogen atmosphere for 12 h. The solution was cooled down to room temperature and the resulting heterodimeric nanoparticles were purified by the addition of ethanol followed by centrifugation. The solids were carefully separated from the supernatant, washed with ethanol and redispersed in hexane containing 1-2.5 µL of oleic acid.
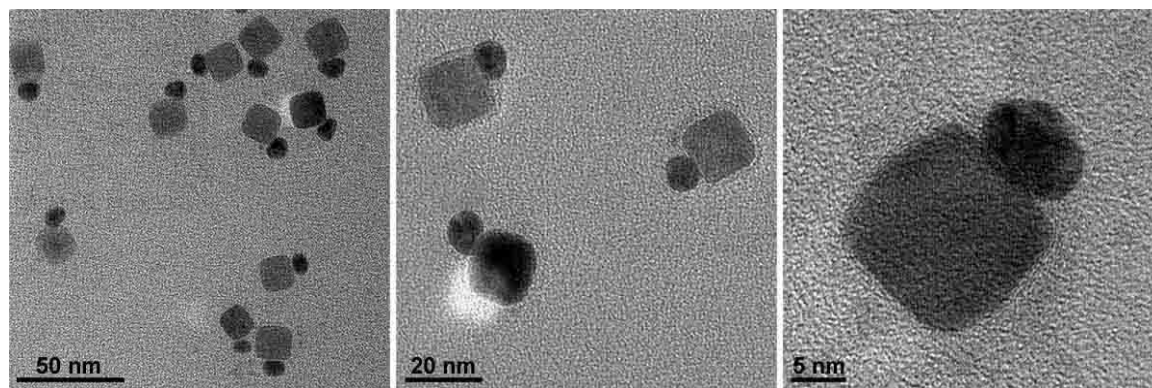

Fig. S7. TEM images of Ag-Fe_3O_4 heterodimers at various magnifications.

S2. Magnetic field-induced self-assembly of nanocrystals at the liquid-air interface

In a typical experiment, a hexane solution of NCs (V = 20 µL; c = 2.5 mg/mL) containing oleic acid (1.25 µL/mL) was placed on the surface of diethylene glycol (DEG) (Aldrich, 99%) (~2 mL) inside a polyethylene well (diameter ≈ 2 cm; height ≈ 1.8 cm) placed between two neodymium magnets. The well was covered with a glass slide and left undisturbed until hexane has evaporated (up to 30 min). A small amount (~200 µL) of acetonitrile was very carefully applied onto the surface of DEG thereby lifting the NC film from the DEG-air interface to acetonitrile-air interface. Finally, the NC film was carefully transferred onto a desired substrate (silicon wafer, carbon-coated TEM grid, etc.). We emphasize that acetonitrile was introduced once the self-assembly process was completed in order to facilitate evaporation of residual solvent (acetonitrile vs. DEG) from the solid substrate. We verified that assemblies identical to those reported here were obtained following direct transfer from the DEG-air interface onto solid substrates, however the high boiling point of DEG (245 °C) made sample preparation cumbersome. We also emphasize that a complete evaporation of hexane in the presence of an applied magnetic field was critical for the formation of well-defined assemblies. No helical NC superstructures could be found, for example, when the magnetic field was removed before the solvent evaporated.

It is important to emphasize the critical role of oleic acid (OA) in the formation of the highly ordered superstructures reported here; in its absence under otherwise identical conditions, the resulting assemblies were short and irregular (see Fig. S8G-I), similar to those reported previously (*40, 41*). As a non-solvent for our NCs (*42, 43*), OA induces attractive vdW (*43*) and/or depletion (*29*) interactions between the NC as hexane (the "good" solvent) gradually evaporates. In pure hexane, no attractive interactions beyond the magnetic dipole-dipole forces

are induced until the volume fraction of the NCs is very high – at which point aggregation commences rapidly, giving rise to ill-defined assemblies (Fig. S8G-I).

Because of a high boiling point (360 °C) of OA, the belts that formed were embedded in a thin film of OA (see, e.g., Fig. S12) and, interestingly, their structure could further be manipulated – e.g. Fig. S13A shows ensembles of belts wrapped together with their OA matrix. At the same time, the OA layer could be dissolved in methanol to leave behind OA-free belts on a solid substrate.

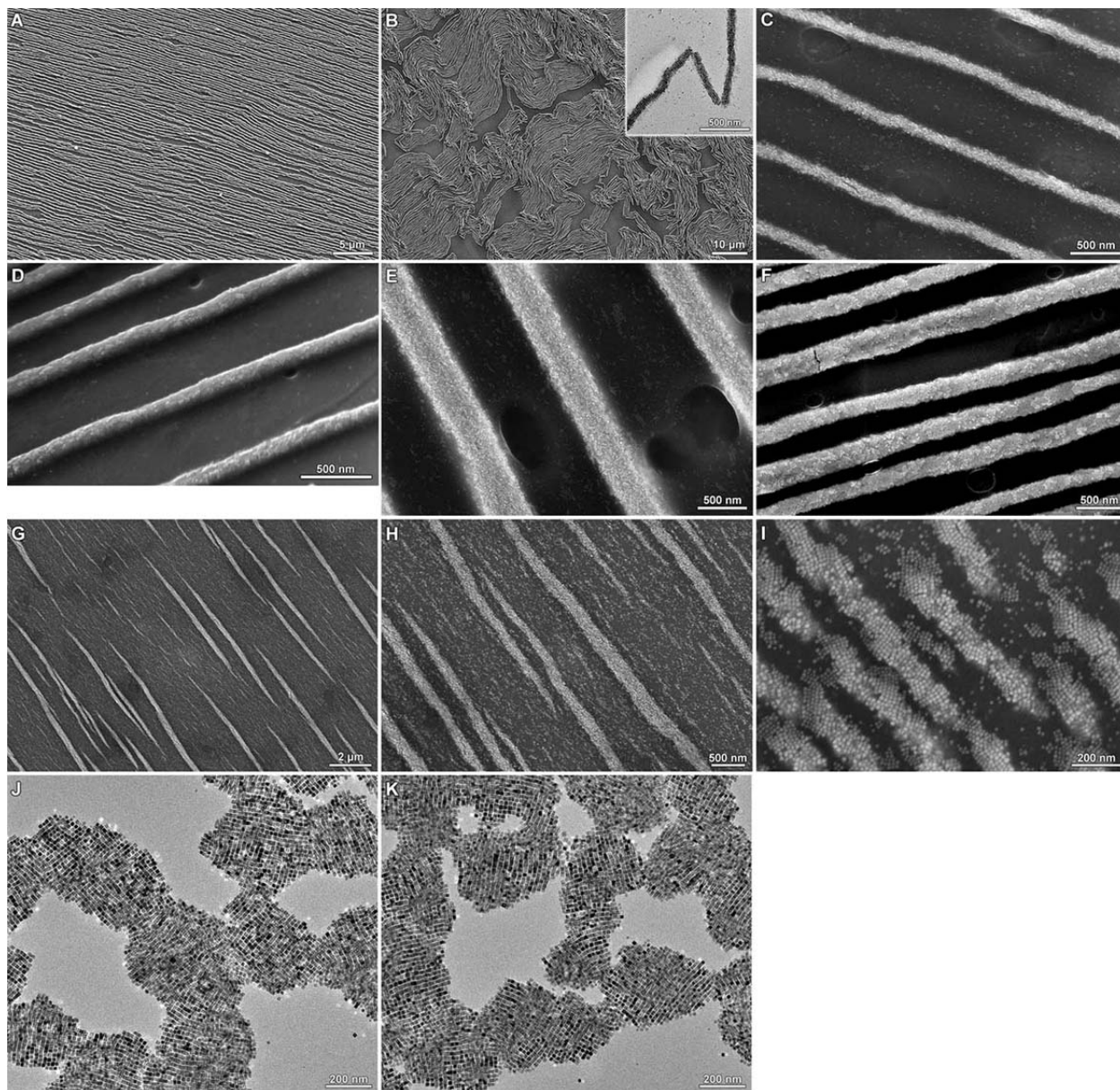**Fig. S8.** (**A-F**) SEM images of belts assembled from Fe_3O_4 nanocubes. The sample in (**B**) was intentionally mishandled while transferring from the liquid-air interface to the solid substrate (silicon wafer / carbon-coated TEM grid). (**D**) is an SEM image taken at a tilt angle of ~45°. Images in (**G-I**) SEM images showing the results of control experiments in which self-assembly

of the nanocubes was performed under conditions identical to those used in (**A-F**), but in the absence of excess oleic acid. (**J**, **K**) TEM images showing the results of control experiments in which self-assembly of the nanocubes was performed under conditions identical to those used in (**A-F**) in the absence of an applied magnetic field.
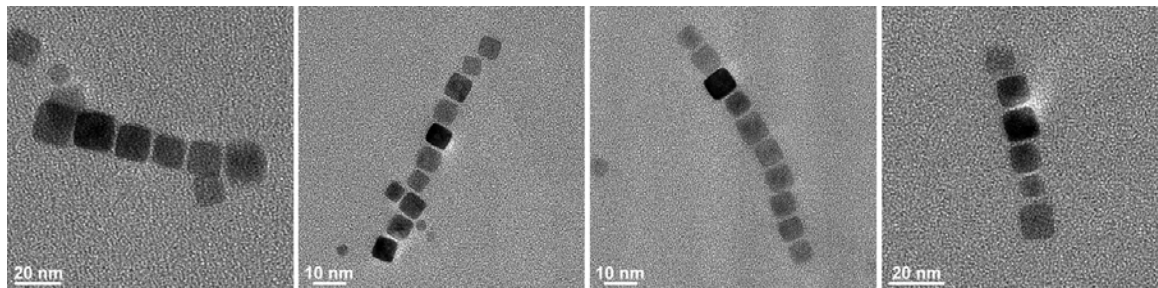
Fig. S9. TEM images of chains of cubic magnetite NCs formed by applying an external magnetic field to a solution of NCs. The samples were prepared by rapid evaporation the solvent (hexane) from the TEM grid in the presence of a magnetic field.

Fig. S10. SEM images of structures obtained from Fe_3O_4 nanocubes under a sub-monolayer ($\chi =$ ~0.2) surface concentration of the particles. All SEM images shown in this manuscript were obtained on a SUPRA 55VP field-emission SEM (Carl Zeiss Microscopy, LLC), or on an ULTRA 55 field-emission SEM (Carl Zeiss Microscopy, LLC, both operating at 5 kV.
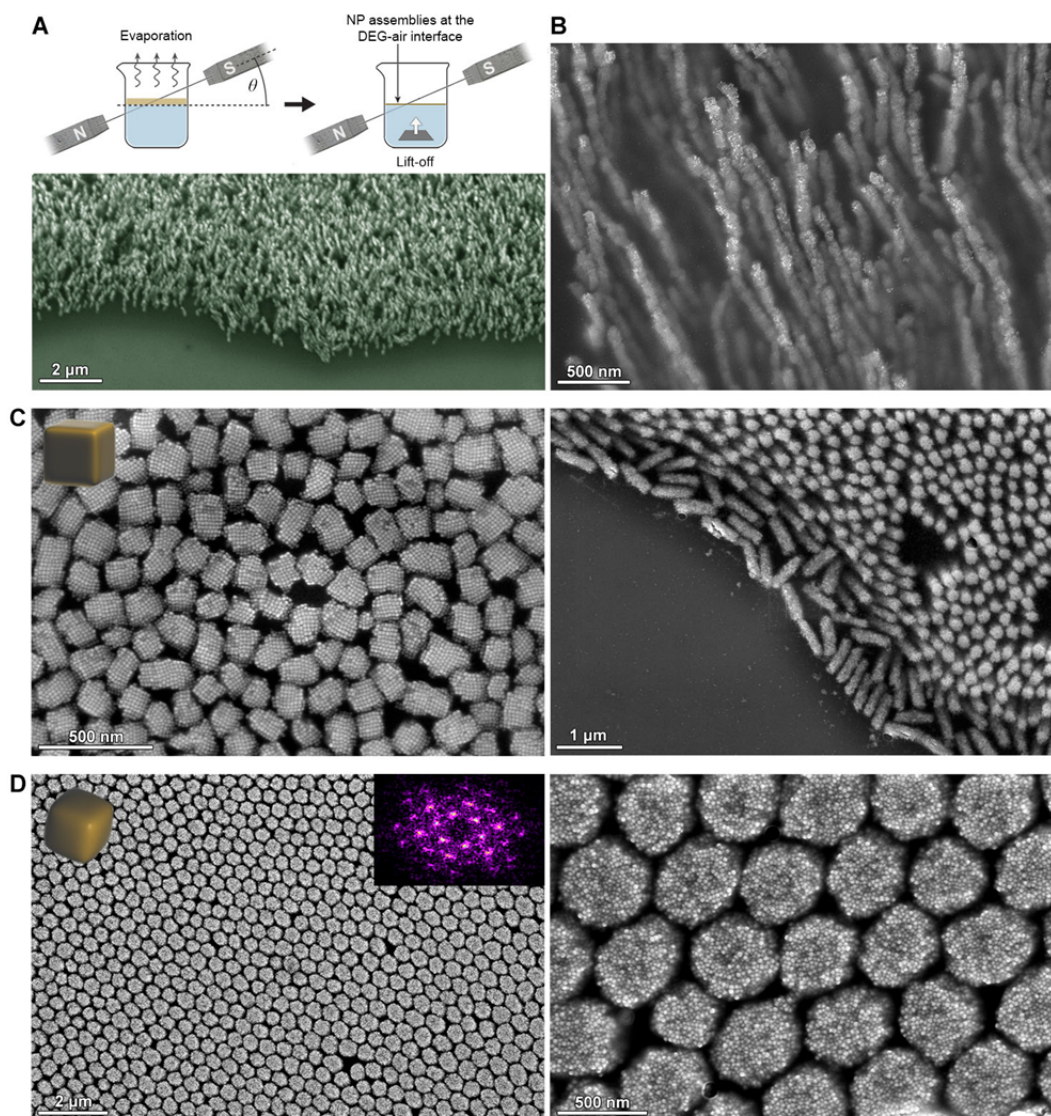
Fig. S11. Effect of tilting the magnetic field away from the direction parallel to the liquid-air interface. (**A**) Schematic representation of the experimental setup. (**B**) SEM ima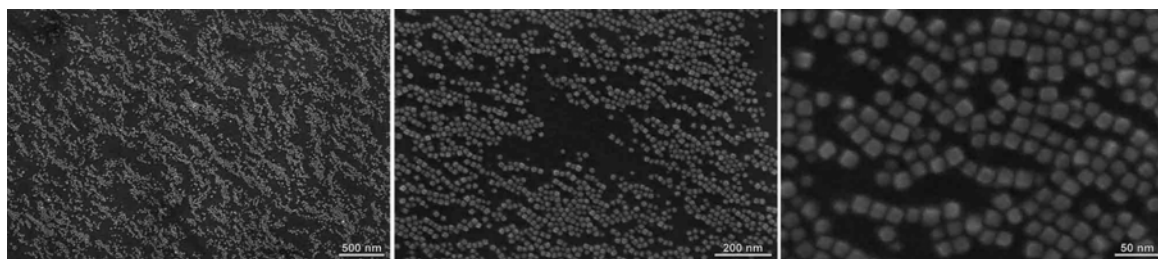ge of belts obtained from Fe$_3$O$_4$ cubes at $\theta \sim 20°$. (**C**) SEM images of pillars obtained from the cubes at $\theta \sim 90°$. Image on the right shows an edge of the sample. (**D**) SEM images of pillars obtained from Fe$_3$O$_4$ rounded cubes at $\theta \sim 90°$. Inset shows a fast Fourier transform (FFT) pattern of the SEM image on the left. We note that no helical assemblies were observed in these experiments, likely because the filaments didn't comprise sufficient number of nanocubes for the effective magnetic field to induce the belt→helix transition.
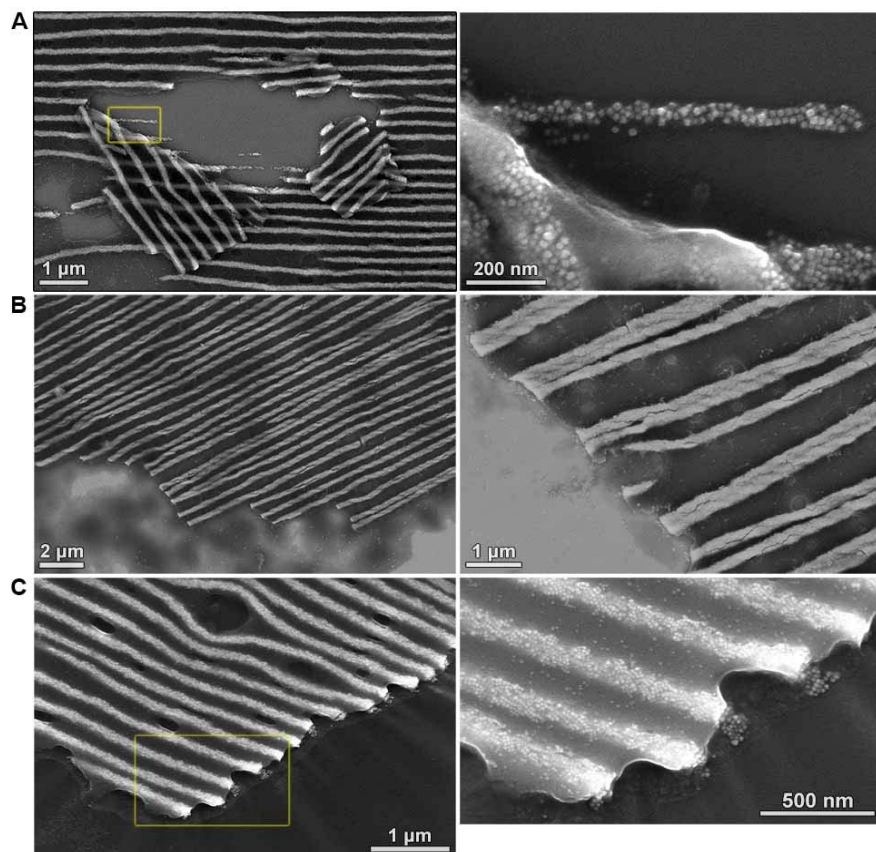
Fig. S12. SEM images showing the presence of the oleic acid film. The area indicated in yellow in (**A**), *left*, is expanded as (**A**), *right*. The area indicated in yellow in (**C**) *left*, is expanded as (**C**), *right*.
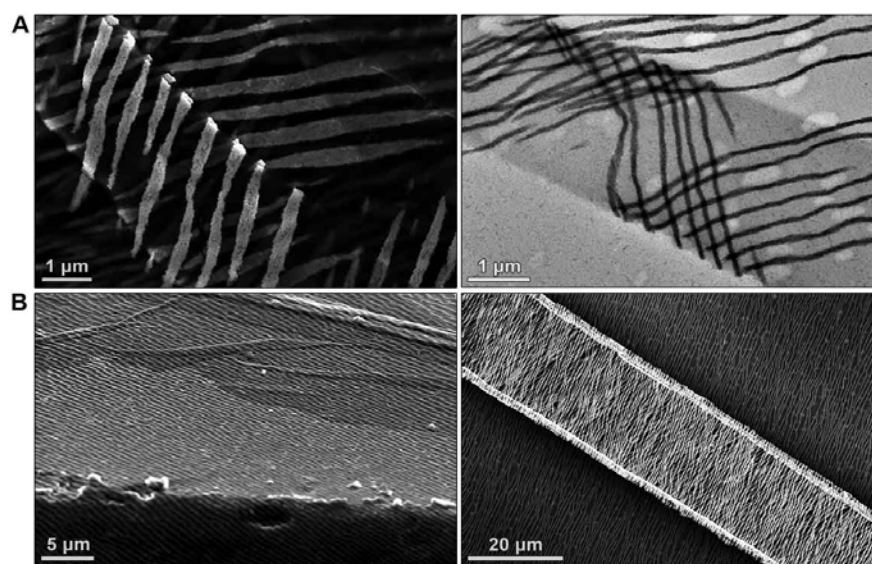
Fig. S13. SEM and TEM images showing folding of (**A**) belts and (**B**) helices along with the oleic acid matrix.
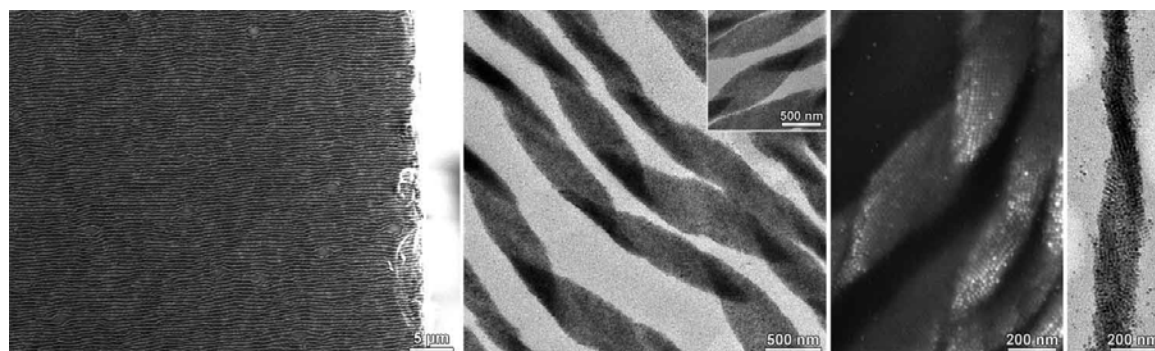
Fig. S14. Additional SEM and TEM images of single-stranded helices. The bright portion of the SEM image on the left indicates the edge of the substrate (silicon wafer).
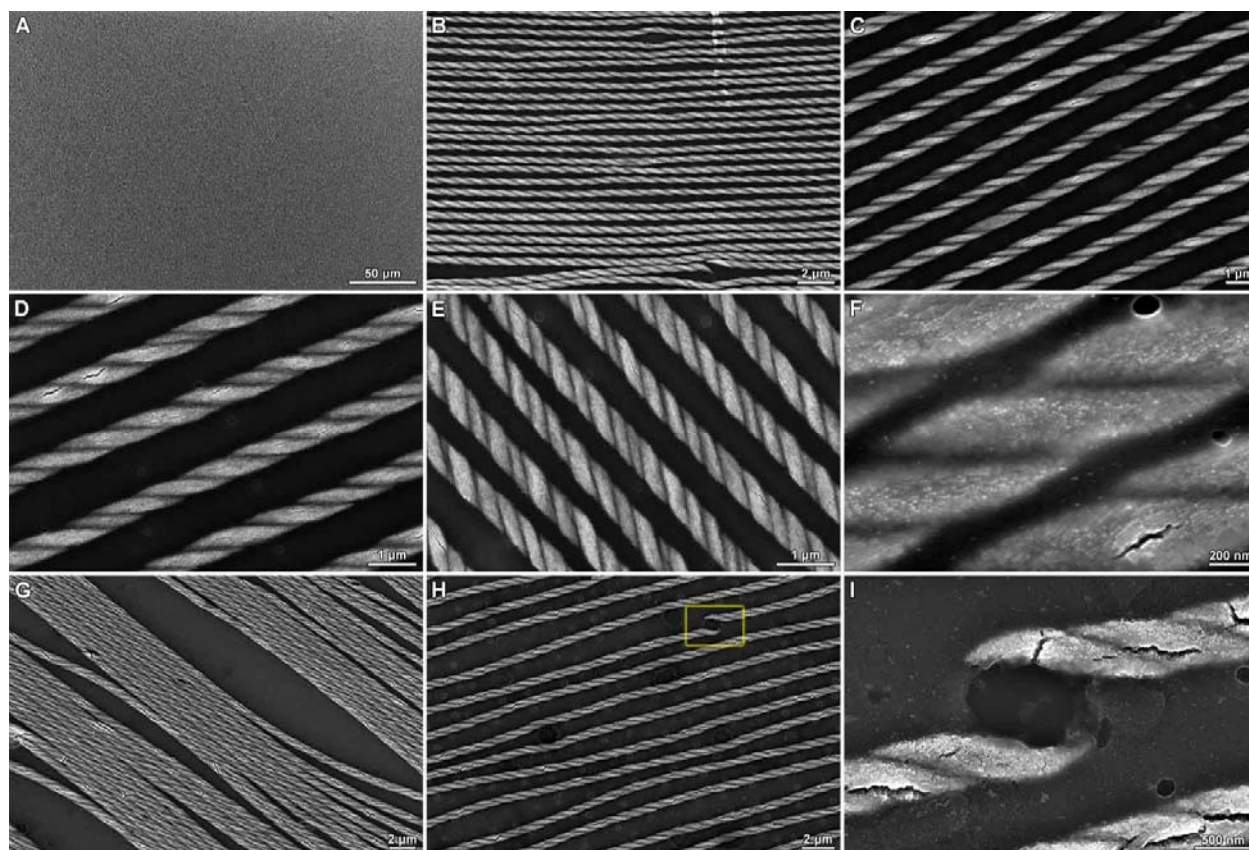
Fig. S15. Additional SEM images of double-stranded helices taken at various magnifications. The area indicated in yellow in (**H**) is expanded as (**I**).
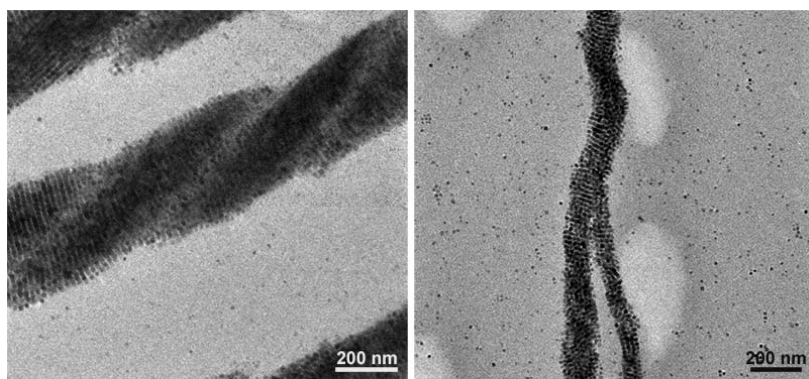
Fig. S16. Additional TEM images of double-stranded helices. The image on the right shows a region where two belts fold to give a double helix.
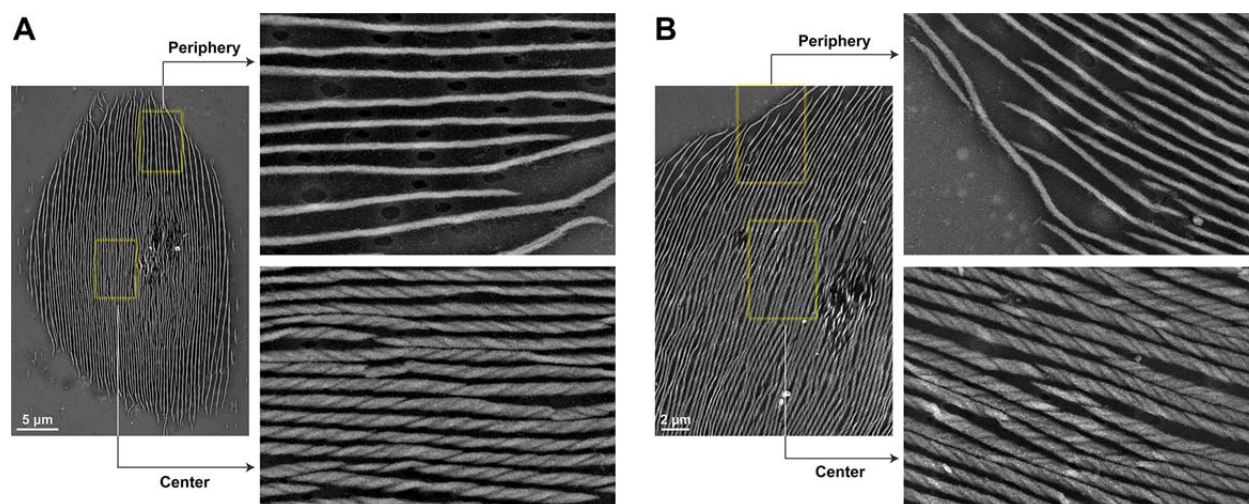
Fig. S17. Dependence of the self-assembled superstructure on the effective magnetic field. Central regions of small patches of filaments (prepared using microdroplets of hexane containing NCs and OA) comprise helical assemblies, which transform into one-dimensional belts at the peripheries of the patches. No helices were found at the terminal positions of the filaments (i.e. helical filaments always unfold at the ends). We attribute these results to varying effective magnetic field throughout the patch: the relatively high density of NC in the center gives rise to an effective field high enough to induce the belt→helix transition. These experiments highlight the importance of the effective magnetic field on the nature of self-assembled superstructures.
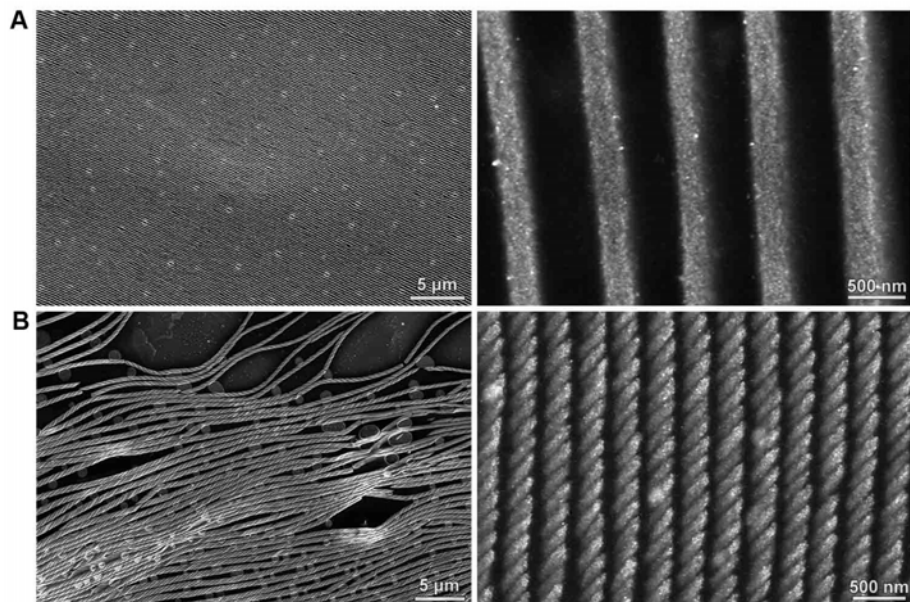
Fig. S18. Additional SEM images of belts (**A**) and helices (**B**) assembled from Ag-Fe$_3$O$_4$ heterodimeric nanoparticles.
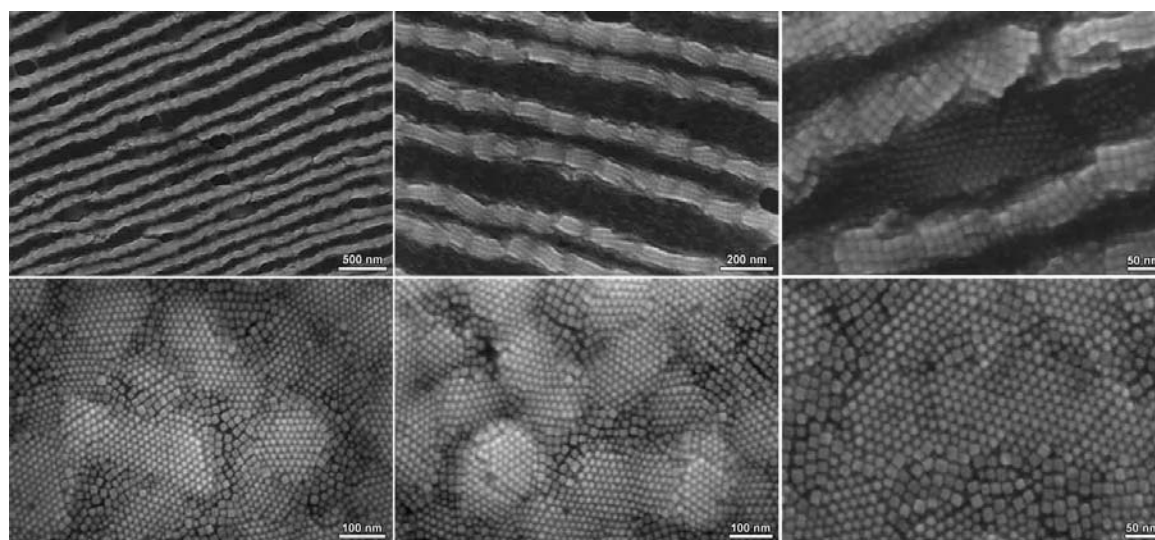
Fig. S19. *Top row:* SEM images of belts prepared from a mixture of ~13 nm Fe$_3$O$_4$ cubes and ~11 nm Fe$_3$O$_4$ spheres, both functionalized with oleic acid. In this case, the cubes assemble selectively while the spheres will empty spaces between them. Bottom row: samples prepared from the same mixture of cubes and spheres but in the absence of an applied magnetic field. No long-range phase-separation is observed.

S3. Monte Carlo simulations

To better understand the nature of the NC superstructures, we model the self-assembly of NCs by separate semi-analytical and Monte Carlo (MC) simulations performed in a canonical ensemble (25). We model the self-assembly of nanocubes functionalized with oleic acid ligands and solvated in hexane with an additional oleic acid, in the presence of external magnetic fields. The nanocubes have coupled mechanical and magnetic degrees of freedom; they interact with each other by van der Waals (vdW) coupling, originating in the NC bulk material, the NC ligands, and the solvent; the super-dipoles, associated with the single magnetic domains of the nanocubes, interact with the external field by the Zeeman coupling, the dipoles of neighboring nanocubes by a dipole-dipole (dd) coupling, the spatial orientations of the nanocubes are defined by shape anisotropy and magnetocrystalline anisotropy (MA) (34–37, 42).

The dynamics of a typical NC self-assembly experiment is controlled by varying competing forces due to changing composition of the system associated with hexane evaporation. Therefore, both thermodynamically and kinetically controlled processes take part in the self-assembly processes. Initially, the ligated nanocubes are well soluble in hexane, and form only short chains (Fig. S9) when the magnetic field is applied. As hexane evaporates, the nanocubes start to coagulate in the remaining OA (42, 43) due to vdW attraction and magnetic coupling. The coagulation is likely enhanced by depletion (entropic) forces and forces related to the gradient of hexane concentration (drying). Eventually, hexane evaporates completely and the self-assembled structures become frozen and partly fractured due to capillary forces from an OA film covering them.

The total energy of NC assemblies, E_T, is defined as the sum of energies related to the above named interactions (equations 1-5 in Section S4). The Zeeman coupling tends to align the dipoles along the field, but MA prefers them to be oriented along the NC body diagonals. The dd-coupling causes attraction between two parallel dipoles when they are within a cone with an azimuthal angle, $\theta < \cos^{-1}(1/\sqrt{3}) \approx 54°$; otherwise, their repulsion takes part. The dd-coupling combines with the external field to form an effective magnetic field, B (magnetic susceptibility), which determines the outcome of the individual magnetic contributions and the types of formed structures: in the presence of a weak B, only short nanocube chains form (e.g. Fig. S10); when B is higher, the nanocubes form thin belts (belts$_{100}$); at even higher B, wide, multilayered belts$_{110}$ are observed; finally, when B are the highest, the assemblies that form show helical features.

First, we study orientations of the magnetic dipole moments in different spatially fixed, perfectly aligned nanocube lattices (see Fig. 1E in the main text). In thin belts$_{100}$ under a relatively weak external magnetic field ($H = 167$ G), the (local) dipoles are on average largely oriented along the belts (Fig. 1E). Here, placing the dipoles above each other strengthens their parallel orientations (attractive dd-coupling). However, in wider belts (unfavorable side-by-side dd-interactions) under the same field, the dipoles tend to form a "zigzag" configuration, which is unlocked from the external field (as the effective field grows), and has an increasing the contribution of MA. Note that the dipoles positioned near belt boundaries are aligned more vertically due to the dominant coupling to the external field. The effect of external field strength is illustrated in Fig. 1D, whereby a zigzag-to-parallel transition of dipoles in a relatively wide belt$_{100}$ is observed under increasing ($H = 167$, 417, and 668 G) external field. In multilayered stripes, the zigzag arrangement occurs in two dimensions, which leads to the formation of an "onion-like" dipole configuration, with counter-propagating fluxes in neighboring flux-closure rings (44, 45) (see Fig. S20).

TOP VIEW
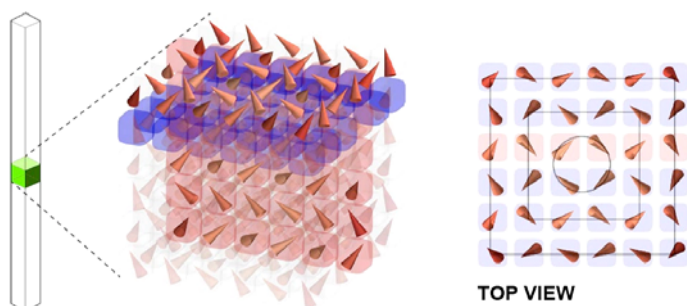
Fig. S20. Averaged orientation of dipoles in a thick filament under relatively weak external field ($H = 167$ G). The top two layers are purposely separated from the structure (*left*) to better illustrate the dipole arrangement.

Next, we compare the relative stability of belt$_{100}$ vs. belt$_{110}$ by MC simulations. In general, the outcome of this competition is determined by the interplay between vdW interactions (disfavor belt$_{110}$ because of the its ridged sides), and magnetic interactions (favor belt$_{110}$ because of the arrangement of individual NCs enabling easy magnetization; large thicknesses and heights of belts entail increasing induced magnetic field, and they favor belts$_{110}$ as observed experimentally). Quantitative analysis of the two types of belts of different thicknesses is shown in Fig. S22.

Despite the favorable arrangement of dipoles in the direction parallel to the long axis of belt$_{110}$, the zigzag configuration is preserved in multilayered belts$_{110}$ in the direction perpendicular to the liquid-air interface. A smooth (non-zigzag) connectivity of the dipoles following the nanocubes' easy axis can be resolved if the structures are further reconfigured by "side-stepping" of the nanocubes, which eventually leads to helical structures.

SIDE VIEW   TOP VIEW
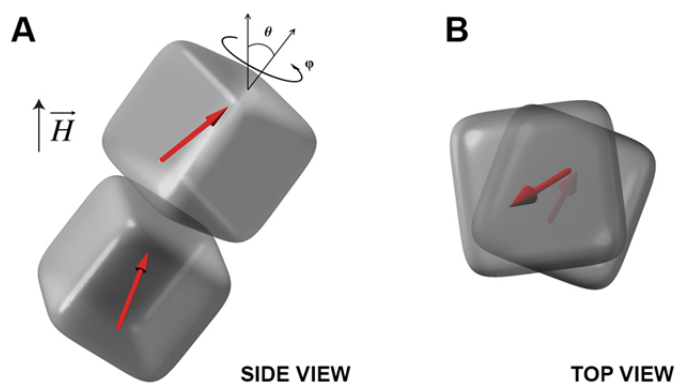
Fig. S21. (A) Typical configuration of two cubes in an external field, $H = 167$ G (vertical z-orientation) at $T = 300$ K (bulk vdW coupling is reduced by ½ with respect to the nominal value). **(B)** View along the cube axis reveals that the nanocube pair is (transiently) chiral. Magnetic dipoles are represented by red arrows.

Figure S21 shows the formation of a transiently chiral nucleus formed by two SPM nanocubes with vdW coupling in a magnetic field. The nanocubes spend most of the time in configurations that possess either left or right chirality, where the tilt angle between the cubes is around ~10-30 degrees. The chirality is the result of a competition between the magnetic and the spatial (nanocube) symmetries. We propose that the propagation of these transiently chiral structures in the presence of many cubes leads to the formation of globally chiral helices.

		$H = 167$ G	$H = 417$ G	$H = 668$ G
3_{100}		$E_{all} = -46.66$	$E_{all} = -50.68$	$E_{all} = -54.78$
		$E_{vdW} = -34.70$	$E_{vdW} = -34.70$	$E_{vdW} = -34.70$
		$E_{mag} = -11.96$	$E_{mag} = -15.98$	$E_{mag} = -20.08$
3_{110}		$E_{all} = -42.80$	$E_{all} = -46.91$	$E_{all} = -51.03$
		$E_{vdW} = -31.64$	$E_{vdW} = -31.64$	$E_{vdW} = -31.64$
		$E_{mag} = -11.16$	$E_{mag} = -15.27$	$E_{mag} = -19.39$
6_{100}		$E_{all} = -51.08$	$E_{all} = -54.83$	$E_{all} = -58.90$
		$E_{vdW} = -38.96$	$E_{vdW} = -38.96$	$E_{vdW} = -38.96$
		$E_{mag} = -12.12$	$E_{mag} = -15.87$	$E_{mag} = -19.94$
6_{110}		$E_{all} = -49.21$	$E_{all} = -53.32$	$E_{all} = -57.44$
		$E_{vdW} = -37.39$	$E_{vdW} = -37.39$	$E_{vdW} = -37.39$
		$E_{mag} = -11.82$	$E_{mag} = -15.93$	$E_{mag} = -20.05$
9_{100}		$E_{all} = -52.57$	$E_{all} = -56.20$	$E_{all} = -60.26$
		$E_{vdW} = -40.38$	$E_{vdW} = -40.38$	$E_{vdW} = -40.38$
		$E_{mag} = -12.19$	$E_{mag} = -15.82$	$E_{mag} = -19.88$
9_{110}		$E_{all} = -51.34$	$E_{all} = -55.44$	$E_{all} = -59.57$
		$E_{vdW} = -39.31$	$E_{vdW} = -39.31$	$E_{vdW} = -39.31$
		$E_{mag} = -12.03$	$E_{mag} = -16.13$	$E_{mag} = -20.26$

3_{100} 3_{110} 6_{100} 6_{110} 9_{100} 9_{110}

Fig. S22. Potential energies of self-assembled belts as a function of belt thickness, arrangement of cubes, and strength of the external field. Total magnetic energy, E_{mag}, is the sum of the Zeeman energy, E_z, dipole-dipole energy, E_{dd}, and anisotropy energy, E_a : $E_{mag} = E_z + E_{dd} + E_a$. Total potential energy, E_{all}, is the sum of total magnetic energy and the van der Waals energy: $E_{all} = E_{vdW} + E_{mag}$. All values are in kcal/mol per nanocube. Averaged orientations of dipoles in different belts (left) are shown for weak external field ($H = 167$ G). The belts comprise the

following numbers of nanocubes, from left to right: 300, 284, 600, 564, 900, 846. All of the energy values and dipole configurations shown in the figure are averaged over 10,000 MC steps.

Figure S23 shows snapshots from MC simulations of nanocube assemblies during the helix formation, and the corresponding energies (Zeeman energy E_z, dipole-dipole energy E_{dd}, anisotropy energy E_a, total magnetic energy $E_{mag} = E_z + E_{dd} + E_a$, van der Waals energy E_{vdW}, and the total potential energy $E_{all} = E_{vdW} + E_{mag}$). The loss of vdW coupling and, to some extent, the Zeeman and dd coupling in helices is compensated by the gain in E_a and the growth of entropy of the looser and more randomly organized NCs (Fig. S23; also seen experimentally, e.g. Fig. 2D in the main text) (these simulations were performed with scaled parameters to yield helices despite the small widths of the filaments; helices formed by thick filaments should be less prone to entropic forces due to stronger effective magnetic fields).
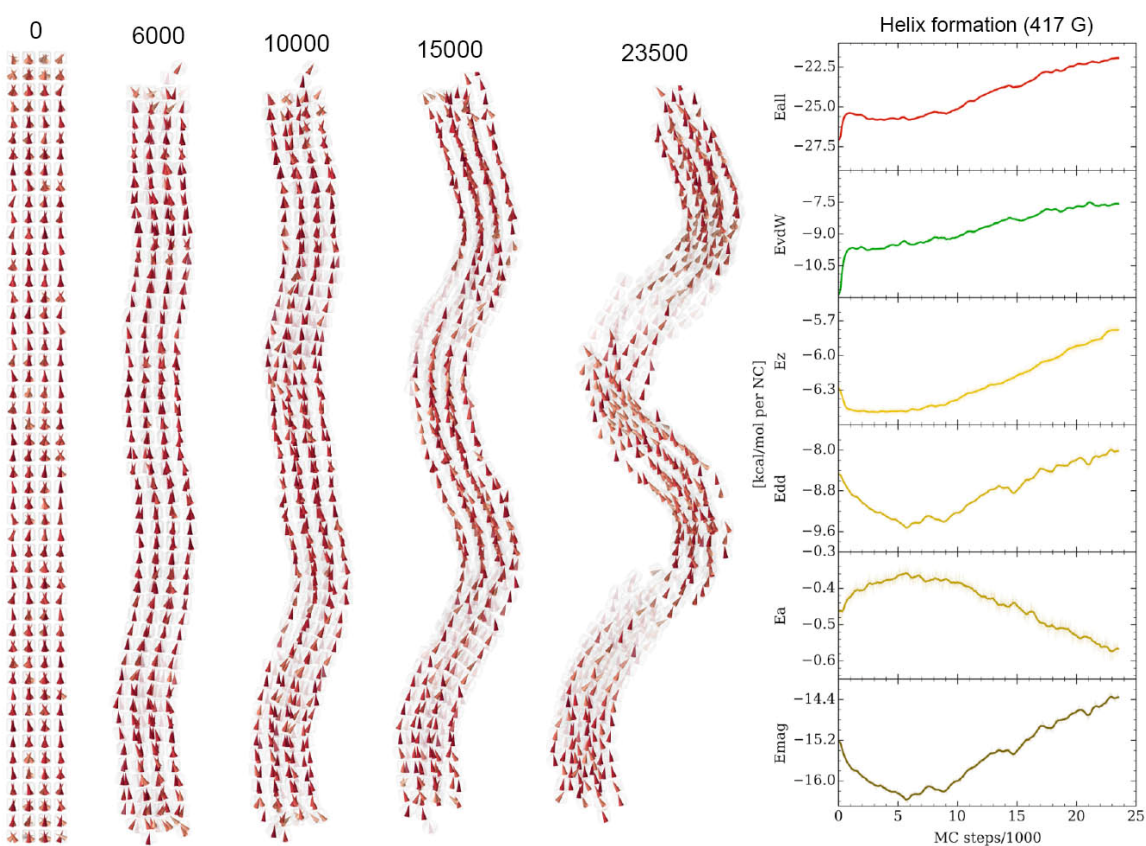
Fig. S23. Snapshots of nanocube assemblies during helix formation (*left*) and the contributing energies (*right*) (E_z, Zeeman energy; E_{dd}, dipole-dipole energy; E_a, anisotropy energy; Emag = E_z + E_{dd} + E_a, total magnetic energy; E_{vdW}, van der Waals energy; $E_{all} = E_{vdW} + E_{mag}$, total potential energy). The curves in the plots were obtained from smoothing (window = 500 steps) the original data (shown as thin lines).

Having discussed the magnetic and spatial structures of individual belts and helices, we examine the formation of their ensembles. The formation of wide ribbons in weak fields signifies the NC

attraction perpendicular to the field direction (*46, 47*). Simulations (Fig. S24) show that two parallel belts attract each other if their dipoles assume zigzag configurations, but they repel each other when the dipoles are largely parallel. Therefore, under weak fields, narrow belts repel each other (parallel dipoles) whereas the wide ones attract (zigzag dipoles). As the external field grows, belts switch their magnetic arrangements from zigzag (attraction) to parallel (repulsion) (Fig. 1D), which stops their widening at high fields, in agreement with the experiments. However, at low fields the "zigzag" belts would widen without limitation, contrary to observations. In reality, introduction of a disorder within the belts (observed experimentally; cf. Fig. S8E) causes the zigzag attraction to be overcome by a mean interfilament repulsion (Fig. S24, *right*). We also modeled a potential energy dependence of two helices as they approach one another to explain the observation of parallel helices (Fig. S15) – Fig. S25 shows that decreasing distance between the helices is associated with their mean magnetic repulsion.
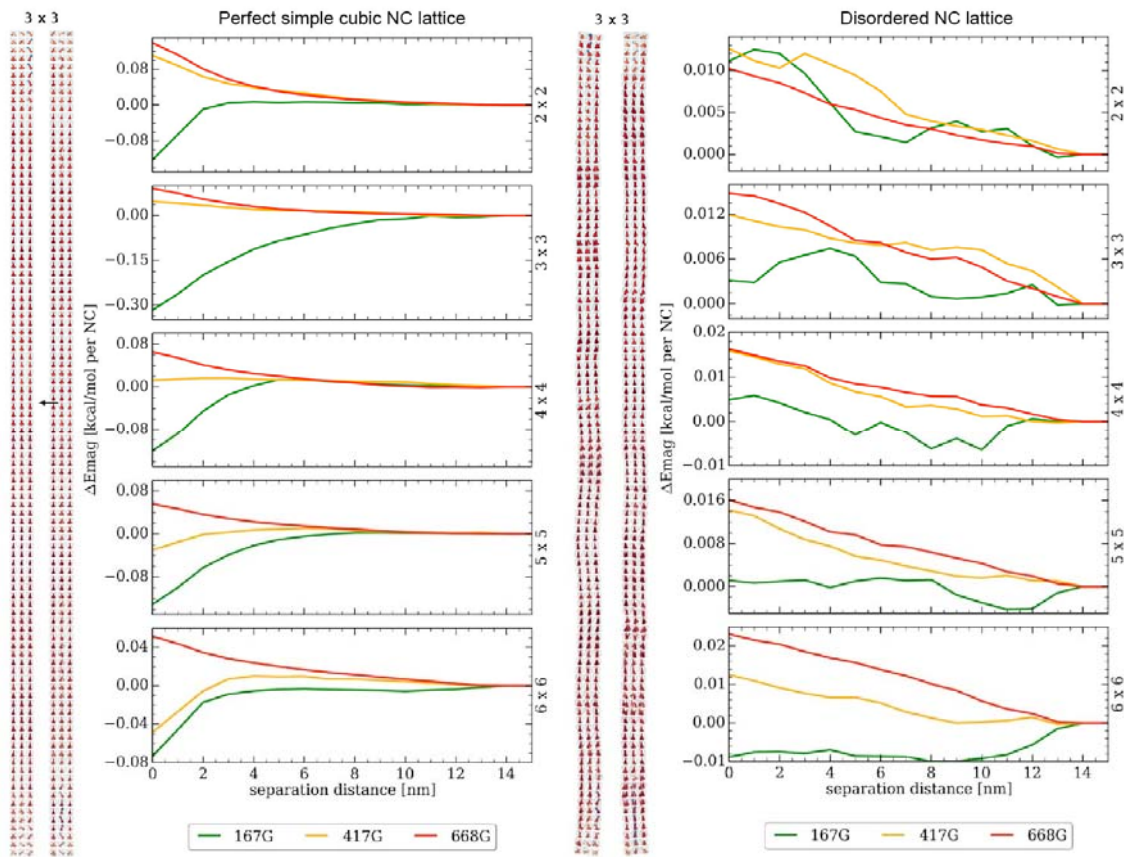
Fig. S24. Potential energy dependence on the distance between two perfectly aligned and slightly disordered belts$_{100}$. In each case, total magnetic energy, $E_{mag} = E_z + E_{dd} + E_a$, was averaged at each distance over 5,000 MC steps of two belts approaching each other as a function of their separation. E_{mag} of two isolated belts was set as zero. The cases of weak, intermediate, and strong external magnetic fields ($H = 167, 417, 688$ G, respectively) are shown for two $n \times n \times 100$ belts, where $n = 2, 3, 4, 5,$ and 6.
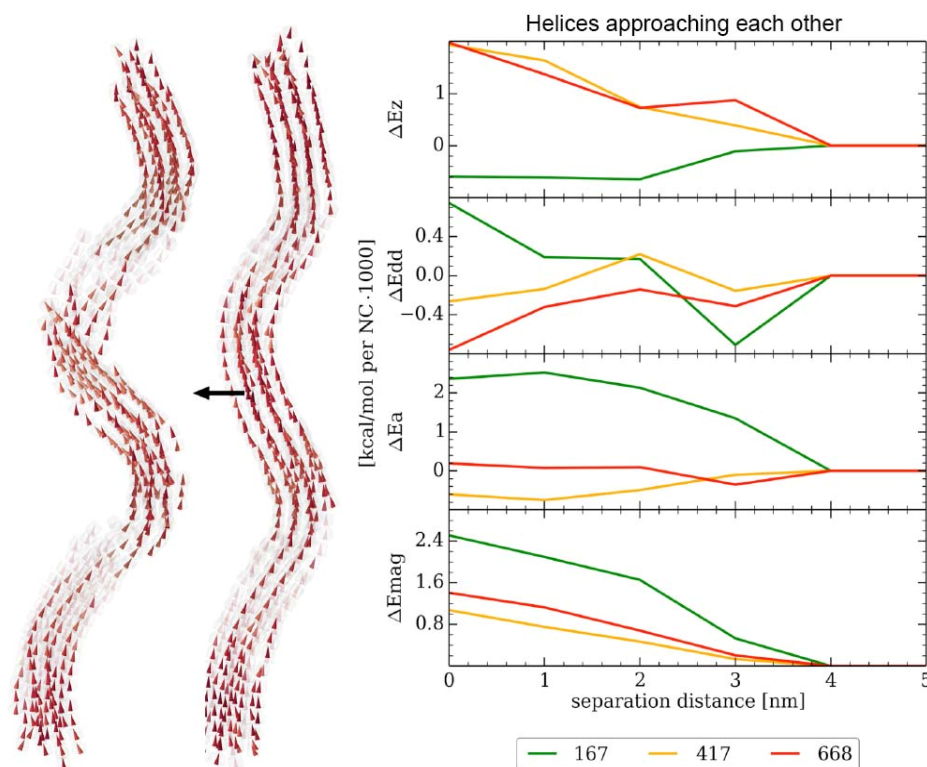
Fig. S25. Potential energy dependence on the distance between two helices approaching each other. Zeeman energy, E_z; dipole-dipole energy, E_{dd}; anisotropy energy, E_a; and total magnetic energy, $E_{mag} = E_z + E_{dd} + E_a$ at each distance were averaged over 5000 MC steps. Colors correspond to different values of the applied magnetic field: 167 G (green), 417 G (yellow), 668 G (red).

Finally, we modeled the behavior of pairs of helices (the last one in Fig. S23) as a function of the phase angle (Fig. S26) and separation distance (Fig. S27), depending on their handedness (the same vs. opposite chirality). The calculations show that the most favorable configuration of two neighboring helices is when they are in phase (i.e., shift angle = 0), irrespective of their reciprocal handedness (Fig. S26). We also found that thin helices of the same handedness repel each other slightly stronger than helices of opposite handedness (Fig. S27).

Fig. S26. Potential energy dependence of helices of the same (*left panel*) and opposite (*right panel*) handedness as a function of the phase angle.
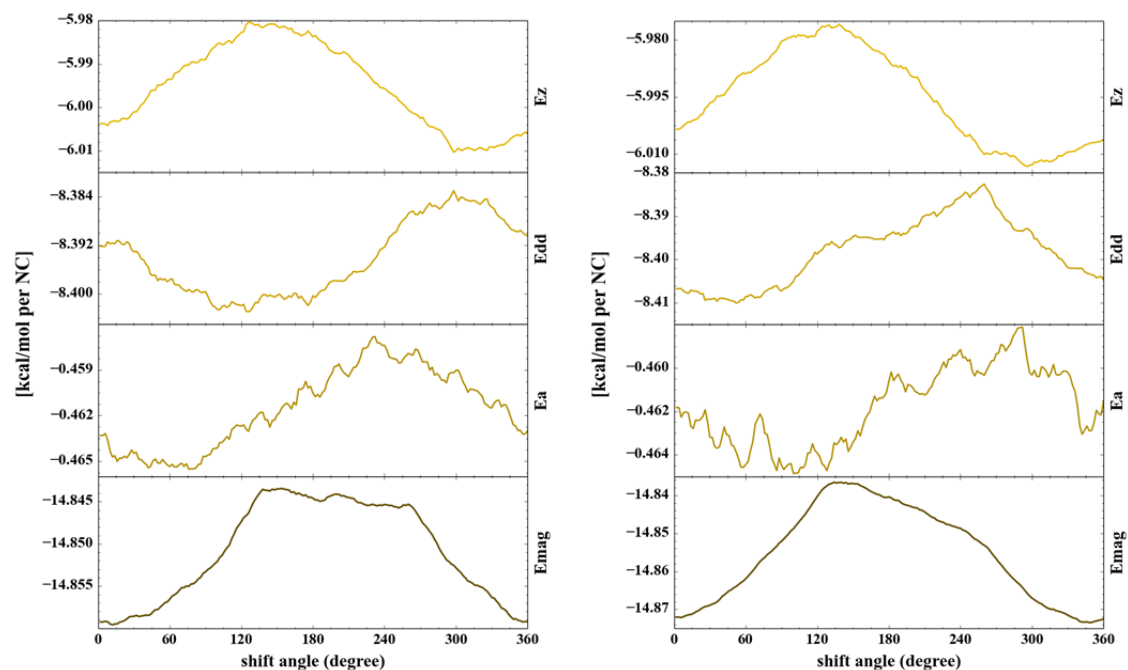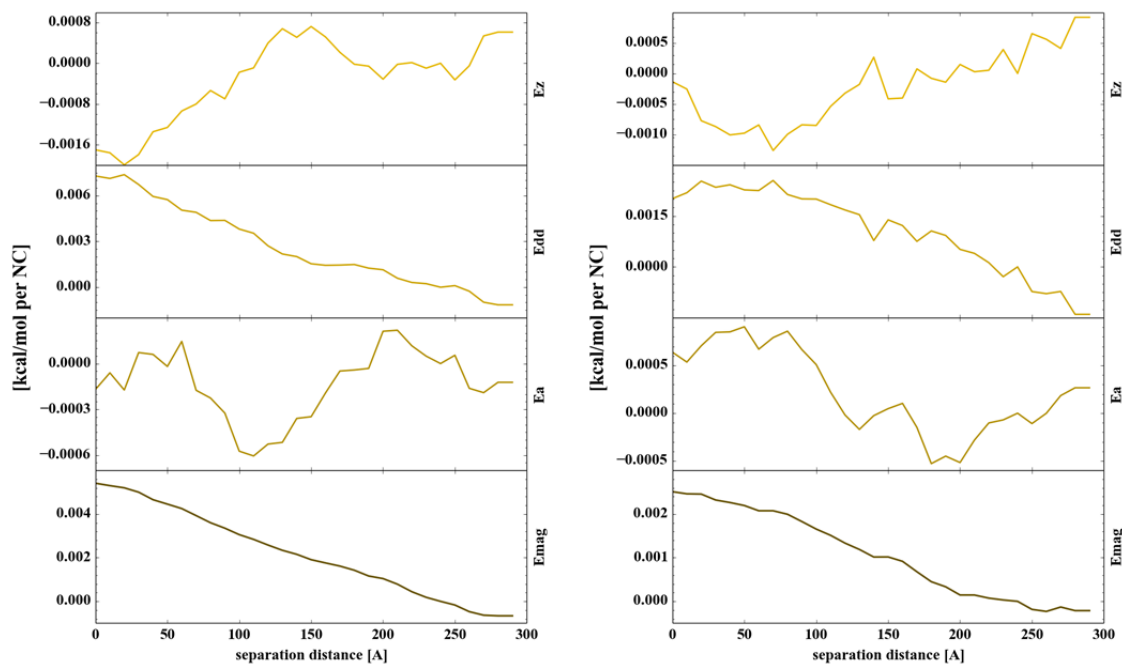

Fig. S27. Magnetic potential energy (in kcal/mol per particle) of helices of the same (*left panel*) and opposite (*right panel*) handedness as a function of reciprocal distance (the helices are parallel). The magnetic interaction energy at large distance is set as zero.

S4. Details of the simulations

At room temperature, small ($d < 26$ nm (*48*)) magnetite nanocubes are superparamagnetic (SPM) (no coercive fields) (*49*). Each nanocube possesses a super-dipole (associated with its single magnetic domain), whose orientation fluctuates at room temperature. In external magnetic fields, the dipole becomes partially locked to the field by Zeeman coupling, and its motion is further constrained by magnetocrystalline anisotropy (MA). For an isolated nanocube, the total energy of such a dipole with a given orientation is given by the sum of its Zeeman and MA energies, $E_i = E_i^Z + E_i^A$. The Zeeman energy is given by

$$E_i^Z = -K_Z(\vec{H} \cdot \overline{M}_i),\tag{1}$$

where $K_z = 1.647 \cdot 10^{-2}$ kcal/mol ($= 2.77 \cdot 10^{-2} \, kT$ at 300 K), $\vec{H} = [0,0,H_0]$ is the external magnetic field vector (in Gauss units), and $E_i^Z = -K_Z(\vec{H} \cdot \overline{M}_i)$ is the magnetic dipole unit vector. In the absence of MA and dipolar coupling with neighboring nanocubes, the field-induced average magnetization of such SPM nanocubes can be described by the Langevin formula, $\langle M \rangle = m_s(\coth(\alpha) - \frac{1}{\alpha})$, where $\alpha = \frac{\mu_0 m_s H}{k_B T}$, m_s is the material-dependent saturation magnetization, H is the applied magnetic field, μ_0 is the magnetic permeability of vacuum, k_B is the Boltzmann constant, and T is the temperature (*50*). However, the MA and dipole-dipole coupling can significantly modify the magnetization.

Bulk magnetite (Fe_3O_4) has an Fd3m crystal structure with quartic and sixth-order anisotropy constants of $K_{A1} = -3.784$ kcal/mol and $K_{A2} = -0.963$ kcal/mol, respectively (*49, 51, 52*). The quartic term is about four times larger than the sixth order term. Therefore, we just use this term to describe the MA energy (*48, 53*),

$$E_i^A = K_{A1}[(M_{ix}' M_{iy}')^2 + (M_{ix}' M_{iz}')^2 + (M_{iy}' M_{iz}')^2],\tag{2}$$

where $M_{ix}', M_{iy}', M_{iz}'$ are the $\hat{x}, \hat{y}, \hat{z}$ components of the magnetic dipole unit vector in the reference nanocube coordinates. The quartic term generates "easy" and "hard" magnetization axes of the nanocubes, which are oriented along the cube body diagonals and edges, respectively. We neglect other corrections of the bulk magnetocrystalline anisotropy energy related to the cubic shape of the nanoparticles (*52, 54*).

The nanocubes interact magnetically with each other by a dipole-dipole (dd) coupling. For simplicity, we represent in our modeling the super-dipole of a single magnetic domain as a point dipole located in the center of each nanocube (*10*). Then, the dd-coupling energy of dipoles in two cubes is given by

$$E_{ij}^{dd} = K_d \left(\frac{\vec{M}_i \cdot \vec{M}_j}{|\vec{r}_{ij}|^3} - \frac{3(\vec{M}_i \cdot \vec{r}_{ij})(\vec{M}_j \cdot \vec{r}_{ij})}{|\vec{r}_{ij}|^5} \right)\tag{3}$$

where $K_d = \mu_0 m_s^2 / 4\pi = 7.973$ kcal/mol, when the distance between dipoles $|\vec{r}_{ij}|$ is measured in units of a, $m_s = Ms \cdot V = 1.174 \cdot 10^{-18}$ A·m^2 is the intrinsic magnetic moment of a homogeneously

magnetized nanocube, where $M_s = 480$ kA/m is the saturation magnetization of a bulk magnetite (*45*) and $V = \frac{2a^3}{\sqrt{\pi}}\Gamma^3(\frac{7}{6}) \approx 0.9a^3$ is the cube volume (*a* is a cuboid length). In reality, the magnetization of nanocubes is not homogeneous due to cubic shape factors (*52, 54*). Moreover, the saturation magnetization of magnetite nanocubes can be significantly smaller than bulk magnetite materials due to disordered spin-glass-like canting spins at the nanocube surface and imperfections in coordination number (*51*). We assume that the saturation magnetization of our nanocubes is ~10-20% smaller than in bulk magnetite due the existence of a disordered surface of an $a \approx 1$ nm thickness (*55, 56*).
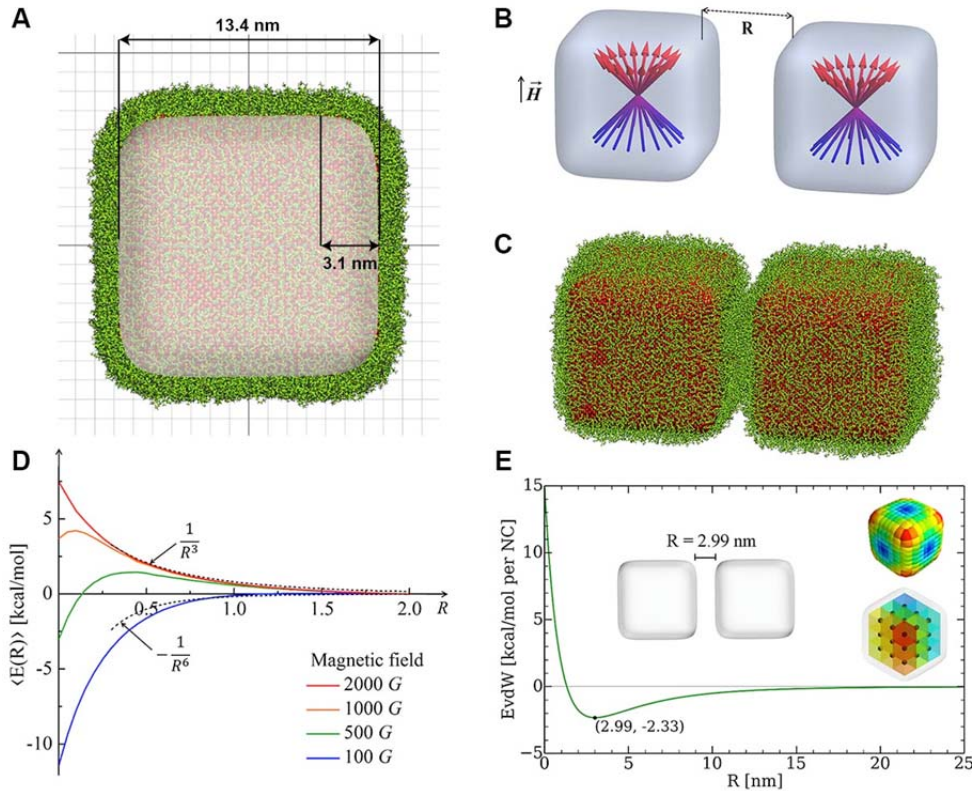
Fig. S28. (**A**) Atomistic model of a single Fe₃O₄ nanocube functionalized with oleic acid ligands. The shape of the inorganic core is based on averaging of multiple TEM images of individual nanocubes. Corner bluntness, ρ, is defined as the ratio of the rounding radius to the side length, and varies between 0% for a perfect cube and 50% for a sphere. (**B**) Two superparamagnetic nanocubes with side length *a* positioned side by side and aligned face-to-face. (**C**) Atomistic model of two nanocubes coated with oleic acid ligands. (**D**) Field-dependent average magnetic energy $\langle E(R) \rangle$ of two nanocubes at temperature, $T = 300$ K. The magnetic energy of two isolated cubes is set as zero. Weak- and strong-field asymptotic dependencies are shown by dashed black lines. (**E**) The effective vdW potential associated with bulk nanocube coupling. *Top inset*: surface elements (color scale from blue to red corresponds to the increase of the surface area per element) used in the repulsive part of the vdW coupling energy (E_W^{rep} in Eqn. 4). *Bottom inset*:

subdivision of a nanocube by 27 identical volume elements (colored for clarity) used in the attractive part of the vdW coupling energy (E_W^{attr} in Eqn. 4).

Eqn. 3 gives the dd-coupling energy of two fixed dipoles. However, the average dd-energy can only be obtained by statistical averaging of Eqn. 3 over thermally accessible dipole orientations (in MC simulations averaging over trajectories), as schematically shown for two nanocubes in a face-to-face arrangement in Fig. S28B. Fig. S28D obtained in this way by semi-analytical simulations shows that the average dd-coupling energy between two fluctuating dipoles positioned side-by-side and affected by the MA and the Zeeman coupling (see Eqn. 6) changes with distance from $-1/R^6$ (attraction) for randomly fluctuating magnetic dipoles (Keesom-like potential, weak-field regime of SPM nanocubes) to $1/R^3$ (repulsion) for strongly coupled ferromagnetic dipoles (*57*) (strong-field regime of SPM nanocubes). At medium field strengths (200-500 G) the R-dependence is non-monotonic with explicit repulsion and attraction regions. When the same calculation is done for nanocubes rotated by 45° with respect to field (cube edge on top) (corresponding to a diamond-like arrangement in Fig. 1E, *right*), the field dependence is similar, except that the repulsion starts at much lower fields (~50-100 G). These results indicate that the simple-cubic lattice arrangement is more "reactive", since neighboring nanocubes can help each other to minimize MA by tilting the dipoles (*58*)

In the MC simulations, the nanocubes are modeled by rigid bodies with a cuboid shape, closely resembling the nanocubes used in experiments, described by a superellipsoid equation $x^6 + y^6 + z^6 = (a/2)^6$, where a = 13.37 nm is the edge length (Fig. S28B). In order to estimate the surface vdW coupling energy of two nanocubes (vacuum), we build an atomistic model of the nanocubes coated with oleic acid (OA) ligands (see Fig. S28C. This ligand-ligand coupling results in a high vdW energy of ~700 kcal/mol per nanocube surface. However, this large surface vdW coupling can only take part upon a complete evaporation of excess OA used as a co-solvent. Since evaporation of OA does not take place under experimental conditions, we cannot use this surface vdW coupling in our MC simulations.

Instead, we describe the non-magnetic coupling between our nanocubes by an anisotropic potential (see Fig. S28E) which includes bulk vdW attraction of the nanocube cores in the OA solvent and the steric repulsion between the surface ligands,

$$E_{ij}^{vdW} = E_{ij}^{attr} + E_{ij}^{rep}, E_W^{attr} = -\varepsilon_1 \frac{A}{\pi^2} \iint_{V_i, V_j} \frac{dV_i dV_j}{r_1^6}, E_W^{rep} = \varepsilon_2 K_W \int_{S_i} \frac{dS_i}{(r_2 + \beta)^8}. \tag{4}$$

The attraction term is a pairwise Hamaker expression (with a scaling constant ε_1), in which the integral is taken over volumes of two interacting nanocubes. Each nanocube is divided into 3^3 = 27 identical volume elements over which the integral (sum) is performed, A = 3 kcal/mol is the Hamaker constant of magnetite in hexane, and r_1 is the distance between the centers of two volume elements in different nanocubes. The repulsion term is expressed as an integral (sum) over 386 surface elements that subdivide the cube's cuboid surface (the elements have different surface areas). Here, r_2 is the distance between the center of a surface element of a chosen nanocube and the surface element of the interacting nanocube. The shape of the vdW potential (Fig. S28E) is tuned by fitting parameters ε_1 = 130, ε_2 = 290, and β = 9.56 nm in a way that the energy minimum of the effective vdW potential is located at the average surface-to-surface

distance of two face-to-face nanocubes, as in experiments (2.99 nm). The strength of the vdW coupling (depth of the potential curve) is defined by a constant of $K_W = \varepsilon_1 \frac{4}{\pi^2}(\frac{0.9a^3}{27})^2 = 2.5 \cdot 10^5 \text{nm}^6$ kcal/mol, which gives a maximum vdW interaction energy of 2.33 kcal/mol per nanocube.

We add the above energy contributions to obtain the total energy of an ensemble of nanocubes,

$$E_T = \sum_{i=1}^{N_P} E_i + \sum_{i=1}^{N_P}\sum_{j=i+1}^{N_P}(E_{ij}^{dd} + E_{ij}^{vdW}). \tag{5}$$

This energy is used in our simulations of the nanocube self-assembly performed with a Markov Chain Monte Carlo (MCMC) algorithm and the Metropolis scheme (*25*). The algorithm uses pseudo-random numbers ("random walks") to generate configuration samples that form a Markov chain. The configuration chain represents a trajectory that should eventually converge to an equilibrium canonical ensemble of nanocube-structure configurations. The expectation values can be obtained by averaging over the equilibrated configurations in the stabilized trajectory. To elucidate magnetic structures for frozen nanocube positions (Fig. S28B), we performed separate semi-analytical simulations, where we averaged over the magnetic energies in a phase space associated with magnetic degrees of freedom,

$$\langle E_T \rangle = \frac{\int E_T e^{-E_T/kT} \Pi_i \, d\Omega_i}{\int e^{-E_T/kT} \Pi_i \, d\Omega_i}. \tag{6}$$

Here, $d\Omega_i = \sin\theta_i \mathrm{d}\theta_i \mathrm{d}\varphi_i$, and θ_i, φ_i are the spherical angles of individual magnetic dipoles in the lab system of coordinates.

In the MC simulations, we compute the total energy difference, ΔE_T, between the system configurations before and after we perform the proposed nanocube or dipole movements. In the Metropolis scheme, a new configuration is accepted when $\Delta E_T \le 0$ or when a random number in the interval [0, 1) is smaller than $e^{-\Delta E_T/kT}$, otherwise the old configuration is kept and the MCMC algorithm proceeds to the next step. In one MCMC cycle, we first vary the values (position and orientation) associated with the mechanical degrees of freedom of every nanocube, and then we perform 10 magnetic steps (local magnetic dipole orientation sampled randomly) for all nanocubes in a random order. We introduce the nanocube translation by a randomly oriented vector and a random length shorter than δs. Likewise, nanocube rotation is performed by moving the nanocube around a randomly oriented axis by a random angle smaller than δa. During the simulation, δs and δa can be changed by 5% (up or down) every 10 cycles in the first 2000 MC cycles and every 1000 MC cycles thereafter to maintain a 50% acceptance rate of the proposed configurations. We achieve uniform sampling in the orientation space by choosing our randomly oriented vectors from a $\mathbf{R}^3$ unit sphere (*59*). This vector selection process is also used to prepare the randomized initial dipole orientation of our simulated systems.

In the simulations, we use the Gilbert–Johnson–Keerthi (GJK) algorithm (*60*) to efficiently determine if two nanocubes overlap. The GJK algorithm can be applied to any convex shapes, once a support function for the particular shape is given. In order to find the support function for our nanocubes, we apply the Lagrange multiplier method with a constraint

equation $x^6 + y^6 + z^6 = (a/2)^6$. The support function for an axis-aligned cuboid-shaped nanocube is given by

$$\text{supp}(\vec{d}) = \frac{\frac{a}{2}}{\sqrt[6]{d_i^{\frac{6}{5}} + d_j^{\frac{6}{5}} + d_k^{\frac{6}{5}}}} \cdot \left[d_i^{\frac{1}{5}}, d_j^{\frac{1}{5}}, d_k^{\frac{1}{5}} \right]. \tag{7}$$

The support function returns a point on the nanocube that is furthest along the direction $\vec{d} = [d_i, d_j, d_k]$. $\text{MinD}(\vec{d}) = \text{supp}_i(\vec{d}_i') - \text{supp}_j(\vec{d}_j')$ gives a boundary point on the Minkowski difference of nanocube i and j, where $\vec{d}_i'$ and $\vec{d}_j'$ are d' projected onto the coordinate of nanocube i and j, respectively. Tetrahedron (3-simplex) formed by four points on boundary of the Minkowski difference will enclose the origin if overlap exists and the enclosure check is done by only a few dot product operations.

Despite the fact that only explicit forces acting on the particles and related energies are used in the MC simulations, the entropy is automatically treated as well. However, the MC code only deals with the configurational entropy of the particles and spins. Other sources of entropy associated with the atomistic nature of the system (solvent, ligands, depletion, etc.) (*1, 61-68*) are not considered in these coarse-grained simulations. Although it would be, in principle, possible to extract an analytical formula for some of these contributions (*66, 69*) such an expression describing two-particle interactions would be hard to implement practically on a model analytical level in the current many-particle system. Recently, entropy was reported as an important factor in the formation of helices under limited conditions [(*70*) and related studies based on colloidal spheres inside thin cylindrical channels]. Another mechanism discussed by Chaikin *et al.* (*71*) demonstrates that helical assemblies of asymmetric dumbbells can result from interplay of magnetic and steric interactions.

S5. Differences and similarities to previously reported helical assemblies of nano- and microparticles

The helical assemblies reported here are unique in that they are prepared from achiral building blocks – iron oxide nanocubes – in sharp contrast to the vast majority of helical assemblies of nanosized particles reported previously, which were made using pre-existing helical templates. These helical templates included peptide amphiphiles (*72, 73*), DNA (*74, 75*), lipids (*76*) and synthetic supramolecular templates (*77*), among others (*78, 79*). A notable exception was reported by Kotov *et al.*, who described an interesting process whereby CdTe nanoparticles self-assembled into complex superstructures, which further evolved into twisted ribbons as a consequence of light-promoted oxidation of telluride ions (*31*). Remarkably, the twist of the ribbons could be controlled by varying irradiation time, but the process led to a roughly equal mixture of right- and left-handed ribbons. Interestingly, as-prepared twisted ribbons could subsequently be converted into helical gold assemblies by the reaction with a gold salt in high yield (*80*).

In larger systems comprising micron-sized colloids, helical assemblies can form when packing frustration is induced. Such frustration can result either from selecting tailor-made particles, or by confining spherical colloids inside thin cylindrical channels. The first strategy is best exemplified by Bibette *et al.* who studied heterodimeric colloidal particles, each comprising

a small paramagnetic domain and a large diamagnetic domain (*71*). In the presence of an external magnetic field, the magnetic domains assembled into one-dimensional chains oriented along the lines of the applied field. The steric bulkiness imposed by the diamagnetic domains forced the assembly to assume a helical structure. The self-assembly of these (*81*) and disc-like ellipsoidal (*82-84*) colloids into helices was also studied theoretically.

Another way to induce packing frustration is to perform inside one-dimensional cylinders having internal diameters not much larger than the diameters of spherical colloids (*85-90*). Notably, sharp transitions between disordered and ordered helical assemblies could be observed upon increasing the volume fraction of the spheres inside thin glass capillaries (*91*). Analogously, spheres confined to the *outer* surface of a cylinder assumed a helical arrangement in order to maximize the commensurability with the cylinder circumference (*92*).

References and Notes

1. E. V. Shevchenko, D. V. Talapin, N. A. Kotov, S. O'Brien, C. B. Murray, Structural diversity in binary nanoparticle superlattices. *Nature* **439**, 55–59 (2006). [Medline](#) [doi:10.1038/nature04414](#)

2. Z. Tang, Z. Zhang, Y. Wang, S. C. Glotzer, N. A. Kotov, Self-assembly of CdTe nanocrystals into free-floating sheets. *Science* **314**, 274–278 (2006). [Medline](#) [doi:10.1126/science.1128045](#)

3. A. M. Kalsin, M. Fialkowski, M. Paszewski, S. K. Smoukov, K. J. Bishop, B. A. Grzybowski, Electrostatic self-assembly of binary nanoparticle crystals with a diamond-like lattice. *Science* **312**, 420–424 (2006). [Medline](#) [doi:10.1126/science.1125124](#)

4. E. Auyeung, T. I. Li, A. J. Senesi, A. L. Schmucker, B. C. Pals, M. O. de la Cruz, C. A. Mirkin, DNA-mediated nanoparticle crystallization into Wulff polyhedra. *Nature* **505**, 73–77 (2014). [Medline](#) [doi:10.1038/nature12739](#)

5. D. Nykypanchuk, M. M. Maye, D. van der Lelie, O. Gang, DNA-guided crystallization of colloidal nanoparticles. *Nature* **451**, 549–552 (2008). [Medline](#) [doi:10.1038/nature06560](#)

6. T. Wang, J. Zhuang, J. Lynch, O. Chen, Z. Wang, X. Wang, D. LaMontagne, H. Wu, Z. Wang, Y. C. Cao, Self-assembled colloidal superparticles from nanorods. *Science* **338**, 358–363 (2012). [Medline](#) [doi:10.1126/science.1224221](#)

7. H. Cui, E. T. Pashuck, Y. S. Velichko, S. J. Weigand, A. G. Cheetham, C. J. Newcomb, S. I. Stupp, Spontaneous and x-ray-triggered crystallization at long range in self-assembling filament networks. *Science* **327**, 555–559 (2010). [Medline](#) [doi:10.1126/science.1182340](#)

8. M. A. Kostiainen, P. Hiekkataipale, A. Laiho, V. Lemieux, J. Seitsonen, J. Ruokolainen, P. Ceci, Electrostatic assembly of binary nanoparticle superlattices using protein cages. *Nat. Nanotechnol.* **8**, 52–56 (2013). [Medline](#) [doi:10.1038/nnano.2012.220](#)

9. K. Miszta, J. de Graaf, G. Bertoni, D. Dorfs, R. Brescia, S. Marras, L. Ceseracciu, R. Cingolani, R. van Roij, M. Dijkstra, L. Manna, Hierarchical self-assembly of suspended branched colloidal nanocrystals into superlattice structures. *Nat. Mater.* **10**, 872–876 (2011). [Medline](#) [doi:10.1038/nmat3121](#)

10. K. J. M. Bishop, C. E. Wilmer, S. Soh, B. A. Grzybowski, Nanoscale forces and their uses in self-assembly. *Small* **5**, 1600–1630 (2009). Medline doi:10.1002/smll.200900358

11. E. V. Shevchenko, D. V. Talapin, S. O'brien, C. B. Murray, Polymorphism in AB(13) nanoparticle superlattices: An example of semiconductor-metal metamaterials. *J. Am. Chem. Soc.* **127**, 8741–8747 (2005). Medline doi:10.1021/ja050510z

12. X. Ye, J. Chen, C. B. Murray, Polymorphism in self-assembled AB6 binary nanocrystal superlattices. *J. Am. Chem. Soc.* **133**, 2613–2620 (2011). Medline doi:10.1021/ja108708v

13. D. Faivre, D. Schüler, Magnetotactic bacteria and magnetosomes. *Chem. Rev.* **108**, 4875–4898 (2008). Medline doi:10.1021/cr078258w

14. R. E. Dunin-Borkowski, M. R. McCartney, R. B. Frankel, D. A. Bazylinski, M. Posfai, P. R. Buseck, Magnetic microstructure of magnetotactic bacteria by electron holography. *Science* **282**, 1868–1870 (1998). Medline doi:10.1126/science.282.5395.1868

15. M. W. Szyndler, R. M. Corn, Self-assembly of flux-closure polygons from magnetite nanocubes. *J. Phys. Chem. Lett.* **3**, 2320–2325 (2012). doi:10.1021/jz300931s

16. M. V. Kovalenko, M. I. Bodnarchuk, R. T. Lechner, G. Hesser, F. Schäffler, W. Heiss, Fatty acid salts as stabilizers in size- and shape-controlled nanocrystal synthesis: The case of inverse spinel iron oxide. *J. Am. Chem. Soc.* **129**, 6352–6353 (2007). Medline doi:10.1021/ja0692478

17. T. Wang, X. Wang, D. LaMontagne, Z. Wang, Z. Wang, Y. C. Cao, Shape-controlled synthesis of colloidal superparticles from nanocubes. *J. Am. Chem. Soc.* **134**, 18225–18228 (2012). Medline doi:10.1021/ja308962w

18. D. Kim, N. Lee, M. Park, B. H. Kim, K. An, T. Hyeon, Synthesis of uniform ferrimagnetic magnetite nanocubes. *J. Am. Chem. Soc.* **131**, 454–455 (2009). Medline doi:10.1021/ja8086906

19. See supplementary materials on *Science* Online.

20. V. Aleksandrovic, D. Greshnykh, I. Randjelovic, A. Frömsdorf, A. Kornowski, S. V. Roth, C. Klinke, H. Weller, Preparation and electrical properties of cobalt-platinum

nanoparticle monolayers deposited by the Langmuir-Blodgett technique. *ACS Nano* **2**, 1123–1130 (2008). Medline doi:10.1021/nn800147a

21. A. Dong, J. Chen, P. M. Vora, J. M. Kikkawa, C. B. Murray, Binary nanocrystal superlattice membranes self-assembled at the liquid-air interface. *Nature* **466**, 474–477 (2010). Medline doi:10.1038/nature09188

22. In that respect, our methodology is akin to Langmuir-Blodgettry of nanocrystals. See also (*23*).

23. Large arrays of stripes assembled from NCs of various compositions were previously prepared by evaporation-induced assembly (*24*); although this method bears some similarity to our results (e.g., NC assemblies were prepared at the liquid-air interface), the mechanism of assembly (based on contact-line instabilities) is conceptually different. In fact, we did not observe the formation of any well-defined structures in the absence of an applied magnetic field (see, e.g., fig. S8J).

24. A. Dong, J. Chen, S. J. Oh, W. K. Koh, F. Xiu, X. Ye, D. K. Ko, K. L. Wang, C. R. Kagan, C. B. Murray, Multiscale periodic assembly of striped nanocrystal superlattice films on a liquid surface. *Nano Lett.* **11**, 841–846 (2011). Medline doi:10.1021/nl104208x

25. S. Brooks, A. Gelman, G. Jones, X.-L. Meng, *Handbook of Markov Chain Monte Carlo* (Chapman & Hall, London, 2011).

26. Z. Kakol, R. N. Pribble, J. M. Honig, Magnetocrystalline anisotropy of $Fe_{3(1-\delta)}O_4$, $0 \leq \delta <$ 0.01. *Solid State Commun.* **69**, 793–796 (1989). doi:10.1016/0038-1098(89)90833-8

27. Ü. Özgür, Y. Alivov, H. Morkoç, Microwave ferrites, part 1: Fundamental properties. *J. Mater. Sci. Mater. Electron.* **20**, 789–834 (2009). doi:10.1007/s10854-009-9923-2

28. The formation of helices, and the self-assembly of NCs in our system in general, is likely facilitated by entropic forces; the large excess of OA used during self-assembly may act as a depletion agent, inducing crystallization of NCs during hexane evaporation as reported previously (*29*).

29. D. Baranov, A. Fiore, M. van Huis, C. Giannini, A. Falqui, U. Lafont, H. Zandbergen, M. Zanella, R. Cingolani, L. Manna, Assembly of colloidal semiconductor nanorods in

solution by depletion attraction. *Nano Lett.* **10**, 743–749 (2010). Medline
doi:10.1021/nl903946n

30. Based on the measurements of electrophoretic mobility [see (*34*)] and the lack of literature
reports on electric dipole moments of magnetite nanoparticles, we did not consider
electrostatic and electric dipole-dipole interactions in our analysis of interparticle
interactions. At the same time, we cannot exclude the possible presence of these
interactions in our system, and leave this possibility open.

31. S. Srivastava, A. Santos, K. Critchley, K. S. Kim, P. Podsiadlo, K. Sun, J. Lee, C. Xu, G. D.
Lilly, S. C. Glotzer, N. A. Kotov, Light-controlled self-assembly of semiconductor
nanoparticles into twisted ribbons. *Science* **327**, 1355–1359 (2010). Medline
doi:10.1126/science.1177218

32. S. Das, P. Ranjan, P. S. Maiti, G. Singh, G. Leitus, R. Klajn, Dual-responsive nanoparticles
and their self-assembly. *Adv. Mater.* **25**, 422–426 (2013). Medline
doi:10.1002/adma.201201734

33. J. V. I. Timonen, M. Latikka, L. Leibler, R. H. A. Ras, O. Ikkala, Switchable static and
dynamic self-assembly of magnetic droplets on superhydrophobic surfaces. *Science* **341**,
253–257 (2013). Medline doi:10.1126/science.1233775

34. Previous self-assembly experiments performed in non-polar solvents excluded a significant
role played by electrostatic interactions [e.g., (*35*, *36*)]. Although the degree of
dissociation of oleic acid (OA) in hexane (dielectric constant = 1.84) is negligible, the
large excess of OA as well as the nature of our experimental setup (self-assembly at the
liquid-air interface) might potentially promote dissociation of OA; to verify this
possibility, we performed electrophoretic mobility, μ_e, measurements (using a Malvern
Zetasizer Nano ZS) of our nanocubes in hexane both in the absence and in the presence
of additional OA (5% *v/v*). The results [0.00706 ($\pm$0.00104)$\cdot 10^{-4}$ cm^2 V^{-1} s^{-1}, and 0.0218
($\pm$0.00710)$\cdot 10^{-4}$ cm^2 V^{-1} s^{-1}, respectively] indicate that in both cases, the nanocubes are
essentially neutral [compare with (*37*)].

35. Z. Chen, J. Moore, G. Radtke, H. Sirringhaus, S. O'Brien, Binary nanoparticle superlattices in the semiconductor-semiconductor system: CdTe and CdSe. *J. Am. Chem. Soc.* **129**, 15702–15709 (2007). Medline doi:10.1021/ja076698z

36. X. Ye, J. Chen, M. Engel, J. A. Millan, W. Li, L. Qi, G. Xing, J. E. Collins, C. R. Kagan, J. Li, S. C. Glotzer, C. B. Murray, Competition of shape and interaction patchiness for self-assembling nanoplates. *Nat. Chem.* **5**, 466–473 (2013). Medline doi:10.1038/nchem.1651

37. S. A. Hasan, D. W. Kavich, J. H. Dickerson, Sacrificial layer electrophoretic deposition of free-standing multilayered nanoparticle films. *Chem. Commun.* **2009**, 3723–3725 (2009). Medline doi:10.1039/b902622c

38. Y. Ridelman, G. Singh, R. Popovitz-Biro, S. G. Wolf, S. Das, R. Klajn, Metallic nanobowls by galvanic replacement reaction on heterodimeric nanoparticles. *Small* **8**, 654–660 (2012). Medline doi:10.1002/smll.201101882

39. L. Zhang, Y. H. Dou, H. C. Gu, Synthesis of Ag-Fe$_3$O$_4$ heterodimeric nanoparticles. *J. Colloid Interface Sci.* **297**, 660–664 (2006). Medline doi:10.1016/j.jcis.2005.11.009

40. Y. Lalatonne, J. Richardi, M. P. Pileni, Van der Waals versus dipolar forces controlling mesoscopic organizations of magnetic nanocrystals. *Nat. Mater.* **3**, 121–125 (2004). Medline doi:10.1038/nmat1054

41. Y. Sahoo, M. Cheon, S. Wang, H. Luo, E. P. Furlani, P. N. Prasad, Field-directed self-assembly of magnetic nanoparticles. *J. Phys. Chem. B* **108**, 3380–3383 (2004). doi:10.1021/jp031148i

42. As previously determined (*43*), ~14 nm iron oxide nanocubes begin to flocculate when the volume fraction of OA in hexane reaches 15-20%.

43. C.-J. Chen, R.-K. Chiang, Y.-R. Jeng, Crystallization and magnetic properties of 3D micrometer-scale simple-cubic maghemite superlattices. *J. Phys. Chem. C* **115**, 18142–18148 (2011). doi:10.1021/jp205635k

44. D. V. Talapin, E. V. Shevchenko, C. B. Murray, A. V. Titov, P. Kral, Dipole-dipole interactions in nanoparticle superlattices. *Nano Lett.* **7**, 1213–1219 (2007). Medline doi:10.1021/nl070058c

45. A. Baskin, W.-Y. Lo, P. Král, Clusters and lattices of particles stabilized by dipolar coupling. *ACS Nano* **6**, 6083–6090 (2012). Medline doi:10.1021/nn301155c

46. T. C. Halsey, Electrorheological fluids. *Science* **258**, 761–766 (1992). Medline doi:10.1126/science.258.5083.761

47. K. Butter, P. H. H. Bomans, P. M. Frederik, G. J. Vroege, A. P. Philipse, Direct observation of dipolar chains in iron ferrofluids by cryogenic electron microscopy. *Nat. Mater.* **2**, 88–91 (2003). Medline doi:10.1038/nmat811

48. K. Abe, Y. Miyamoto, S. Chikazumi, Magnetocrystalline anisotropy of low-temperature phase of magnetite. *J. Phys. Soc. Jpn.* **41**, 1894–1902 (1976). doi:10.1143/JPSJ.41.1894

49. T. K. McNab, R. A. Fox, A. J. F. Boyle, Some magnetic properties of magnetite (Fe_3O_4) microcrystals. *J. Appl. Phys.* **39**, 5703–5711 (1968). doi:10.1063/1.1656035

50. E. M. Claesson, B. H. Erne, I. A. Bakelaar, B. W. M. Kuipers, A. P. Philipse, Measurement of the zero-field magnetic dipole moment of magnetizable colloidal silica spheres. *J. Phys. Condens. Matter* **19**, 036105 (2007). doi:10.1088/0953-8984/19/3/036105

51. H. El Ghandoor, H. M. Zidan, M. M. H. Khalil, M. I. M. Ismail, Synthesis and some physical properties of magnetite (Fe_3O_4) nanoparticles. *Int. J. Electrochem. Sci.* **7**, 5734–5745 (2012).

52. M. E. Schabes, H. N. Bertram, Magnetization processes in ferromagnetic cubes. *J. Appl. Phys.* **64**, 1347–1357 (1988). doi:10.1063/1.341858

53. L. Landau, E. Lifshitz, L. Pitaevskii, *Electrodynamics of Continuous Media* (Butterworth-Heinemann, Oxford, 1984), vol. 8.

54. S. P. Gubin *et al.*, *Magnetic Nanoparticles* (Wiley-VCH, Weinheim, Germany, 2009).

55. M. P. Morales, S. Veintemillas-Verdaguer, M. I. Montero, C. J. Serna, A. Roig, L. Casas, B. Martínez, F. Sandiumenge, Surface and internal spin canting in γ-Fe_2O_3 nanoparticles. *Chem. Mater.* **11**, 3058–3064 (1999). doi:10.1021/cm991018f

56. S. Linderoth, P. V. Hendriksen, F. Bo

57. P. C. Scholten, D. L. A. Tjaden, Mutual attraction of super-paramagnetic particles. *J. Colloid Interface Sci.* **73**, 254–255 (1980). [doi:10.1016/0021-9797(80)90144-7](doi:10.1016/0021-9797(80)90144-7)

58. Although the electric and magnetic dipole-dipole couplings are described formally in the same way, because of the different relative values of interaction parameters describing practical systems, the same regimes cannot be easily prepared in both types of materials.

59. G. Marsaglia, Choosing a point from the surface of a sphere. *Ann. Math. Stat.* **43**, 645–646 (1972). doi:10.1214/aoms/1177692644

60. P. Lindemann, *Algorithms in Media Informatics*, 1-4 (2009).

61. L. V. Woodcock, Entropy difference between the face centered cubic and hexagonal close-packed crystal structures. *Nature* **385**, 141–143 (1997). [doi:10.1038/385141a0](doi:10.1038/385141a0)

62. Z. Cheng, W. B. Russel, P. M. Chaikin, Controlled growth of hard-sphere colloidal crystals. *Nature* **401**, 893–895 (1999). [doi:10.1038/46721](doi:10.1038/46721)

63. M. D. Eldridge, P. A. Madden, D. Frenkel, Entropy-driven formation of a superlattice in a hard-sphere binary mixture. *Nature* **365**, 35–37 (1993). [doi:10.1038/365035a0](doi:10.1038/365035a0)

64. S. C. Glotzer, M. J. Solomon, Anisotropy of building blocks and their assembly into complex structures. *Nat. Mater.* **6**, 557–562 (2007). Medline doi:10.1038/nmat1949

65. Y. Snir, R. D. Kamien, Entropically driven helix formation. *Science* **307**, 1067 (2005). Medline doi:10.1126/science.1106243

66. G. van Anders, N. K. Ahmed, R. Smith, M. Engel, S. C. Glotzer, Entropically patchy particles: Engineering valence through shape entropy. *ACS Nano* **8**, 931–940 (2014). Medline [doi:10.1021/nn4057353](doi:10.1021/nn4057353)

67. K. L. Young, M. L. Personick, M. Engel, P. F. Damasceno, S. N. Barnaby, R. Bleher, T. Li, S. C. Glotzer, B. Lee, C. A. Mirkin, A directional entropic force approach to assemble anisotropic nanoparticles into superlattices. *Angew. Chem. Int. Ed.* **52**, 13980–13984 (2013). Medline doi:10.1002/anie.201306009

68. Y. Zhang, F. Lu, D. van der Lelie, O. Gang, Continuous phase transformation in nanocube assemblies. *Phys. Rev. Lett.* **107**, 135701 (2011). Medline doi:10.1103/PhysRevLett.107.135701

69. G. van Anders, N. K. Ahmed, D. Klotsa, M. Engel, S. C. Glotzer, arXiv 1309.1187 (2013).

70. Y. Yin, Y. Xia, Self-assembly of spherical colloids into helical chains with well-controlled handedness. *J. Am. Chem. Soc.* **125**, 2048–2049 (2003). Medline doi:10.1021/ja029408h

71. D. Zerrouki, J. Baudry, D. Pine, P. Chaikin, J. Bibette, Chiral colloidal clusters. *Nature* **455**, 380–382 (2008). Medline doi:10.1038/nature07237

72. C.-L. Chen, P. Zhang, N. L. Rosi, A new peptide-based method for the design and synthesis of nanoparticle superstructures: Construction of highly ordered gold nanoparticle double helices. *J. Am. Chem. Soc.* **130**, 13555–13557 (2008). Medline doi:10.1021/ja805683r

73. C. Song, M. G. Blaber, G. Zhao, P. Zhang, H. C. Fry, G. C. Schatz, N. L. Rosi, Tailorable plasmonic circular dichroism properties of helical nanoparticle superstructures. *Nano Lett.* **13**, 3256–3261 (2013). Medline doi:10.1021/nl4013776

74. J. Sharma, R. Chhabra, A. Cheng, J. Brownell, Y. Liu, H. Yan, Control of self-assembly of DNA tubules through integration of gold nanoparticles. *Science* **323**, 112–116 (2009). Medline doi:10.1126/science.1165831

75. A. Kuzyk, R. Schreiber, Z. Fan, G. Pardatscher, E. M. Roller, A. Högele, F. C. Simmel, A. O. Govorov, T. Liedl, DNA-based self-assembly of chiral plasmonic nanostructures with tailored optical response. *Nature* **483**, 311–314 (2012). Medline doi:10.1038/nature10889

76. Y. M. Lvov, R. R. Price, J. V. Selinger, A. Singh, M. S. Spector, J. M. Schnur, Imaging nanoscale patterns on biologically derived microstructures. *Langmuir* **16**, 5932–5935 (2000). doi:10.1021/la000069k

77. S. H. Jung, J. Jeon, H. Kim, J. Jaworski, J. H. Jung, Chiral arrangement of achiral Au nanoparticles by supramolecular assembly of helical nanofiber templates. *J. Am. Chem. Soc.* **136**, 6446–6452 (2014). Medline doi:10.1021/ja5018199

78. Y. Zhou, Q. Ji, M. Masuda, S. Kamiya, T. Shimizu, Helical arrays of CdS nanoparticles tracing on a functionalized chiral template of glycolipid nanotubes. *Chem. Mater.* **18**, 403–406 (2006). doi:10.1021/cm051928z

79. S. Guha, M. G. B. Drew, A. Banerjee, Construction of helical nanofibers from self-assembling pseudopeptide building blocks: Modulating the handedness and breaking the helicity. *Small* **4**, 1993–2005 (2008). [Medline](#) [doi:10.1002/smll.200800002](#)

80. G. D. Lilly, A. Agarwal, S. Srivastava, N. A. Kotov, Helical assemblies of gold nanoparticles. *Small* **7**, 2004–2009 (2011). [Medline](#) [doi:10.1002/smll.201100536](#)

81. D. Chakrabarti, S. N. Fejer, D. J. Wales, Rational design of helical architectures. *Proc. Natl. Acad. Sci. U.S.A.* **106**, 20164–20167 (2009). [doi:10.1073/pnas.0906676106](#)

82. D. Chakrabarti, D. J. Wales, Tilted and helical columnar phases for an axially symmetric discoidal system. *Phys. Rev. Lett.* **100**, 127801 (2008). [Medline](#) [doi:10.1103/PhysRevLett.100.127801](#)

83. S. N. Fejer, D. Chakrabarti, D. J. Wales, Self-assembly of anisotropic particles. *Soft Matter* **7**, 3553–3564 (2011). [doi:10.1039/c0sm01289k](#)

84. P. Prybytak, W. J. Frith, D. J. Cleaver, Hierarchical self-assembly of chiral fibres from achiral particles. *Interface Focus* **2**, 651–657 (2012). [Medline](#) [doi:10.1098/rsfs.2011.0104](#)

85. R. O. Erickson, Tubular packing of spheres in biological fine structure. *Science* **181**, 705–716 (1973). [Medline](#) [doi:10.1126/science.181.4101.705](#)

86. M. Tymczenko, L. F. Marsal, T. Trifonov, I. Rodriguez, F. Ramiro-Manzano, J. Pallares, A. Rodriguez, R. Alcubilla, F. Meseguer, Colloidal crystal wires. *Adv. Mater.* **20**, 2315–2318 (2008). [doi:10.1002/adma.200701526](#)

87. G. T. Pickett, M. Gross, H. Okuyama, Spontaneous chirality in simple systems. *Phys. Rev. Lett.* **85**, 3652–3655 (2000). [Medline](#) [doi:10.1103/PhysRevLett.85.3652](#)

88. A. Mughal, H. K. Chan, D. Weaire, S. Hutzler, Dense packings of spheres in cylinders: Simulations. *Phys. Rev. E* **85**, 051305 (2012). [Medline](#) [doi:10.1103/PhysRevE.85.051305](#)

89. A. Mughal, Screw symmetry in columnar crystals. *Philos. Mag.* **93**, 4070–4077 (2013). [doi:10.1080/14786435.2013.817691](#)

90. L. Jiang, J. W. de Folter, J. Huang, A. P. Philipse, W. K. Kegel, A. V. Petukhov, Helical colloidal sphere structures through thermo-reversible co-assembly with molecular

microtubes. *Angew. Chem. Int. Ed.* **52**, 3364–3368 (2013). [Medline](#)
[doi:10.1002/anie.201209767](#)

91. M. A. Lohr, A. M. Alsayed, B. G. Chen, Z. Zhang, R. D. Kamien, A. G. Yodh, Helical packings and phase transformations of soft spheres in cylinders. *Phys. Rev. E* **81**, 040401 (2010). [Medline](#) [doi:10.1103/PhysRevE.81.040401](#)

92. D. A. Wood, C. D. Santangelo, A. D. Dinsmore, Self-assembly on a cylinder: A model system for understanding the constraint of commensurability. *Soft Matter* **9**, 10016–10024 (2013). [doi:10.1039/c3sm51735g](#)